Assessing the impact of diagenesis on foraminiferal geochemistry from a low latitude, shallow-water drift deposit

Assessing the impact of diagenesis on foraminiferal geochemistry from a low latitude, shallow-water drift deposit

Stephanie Stainbank[a], Silvia Spezzaferri[a], Eva De Boever[a,1], Anne-Sophie Bouvier[b], Colin Chilcott[c], Erica S de Leau[c], Anneleen Foubert[a], Tereza Kunkelova[c,2], Laetitia Pichevin[c], Jacek Raddatz[d,e], Andres Rüggeberg[a], James D Wright[f], Siyao M Yu[f], Manlin Zhang[c,3], Dick Kroon[c]

[a]Department of Geosciences, University of Fribourg, Chemin du Musée 6, 1700 Fribourg, Switzerland

[b]Institute of Earth Sciences, University of Lausanne, Géopolis, 1015 Lausanne, Switzerland

[c]School of GeoSciences, University of Edinburgh, Grant Institute, The King's Buildings, James Hutton Road, EH9 3FE Edinburgh, United Kingdom

[d]Institute of Geosciences, Goethe University Frankfurt, Altenhöferallee 1, 60438 Frankfurt, Germany

[e]Frankfurt Isotope and Element Research Center (FIERCE), Goethe University Frankfurt, Altenhöferallee 1, 60438 Frankfurt, Germany

[f]Department of Earth and Planetary Sciences, Rutgers, the State University of New Jersey, Bush Campus, 610 Taylor Road, Piscataway, NJ 08854-8066, USA

[1]Present address: TNO, Geological Survey of the Netherlands, Princetonlaan 6, 3584 CB Utrecht, the Netherlands

[2]Present address: National Oceanography Centre Southampton, University of Southampton, Waterfront Campus, European Way, SO14 3ZH Southampton, United Kingdom

[3]Present address: Faculty of Life Science, University of Bradford, Richmond Rd, BD7 1DP Bradford, United Kingdom

Corresponding author e-mail: stephanie.hayman@unifr.ch

Key words: foraminifera; early diagenesis; tropical drift deposits; stable isotopes; Mg/Ca; IODP

ABSTRACT

Due to their large heat and moisture storage capabilities, the tropics are fundamental in modulating both regional and global climate. Furthermore, their thermal response during past extreme warming periods, such as super interglacials, is not fully resolved. In this regard, we present high-resolution (analytical) foraminiferal geochemical ($\delta^{18}O$ and Mg/Ca) records for the last 1800 kyr from the shallow (487 m) Inner Sea drift deposits of the Maldives archipelago in the equatorial Indian Ocean. Considering the diagenetic susceptibility of these proxies, in carbonate-rich environments, we assess the integrity of a suite of commonly used planktonic and benthic foraminifera geochemical datasets (*Globigerinoides ruber* (white), *Globigerinita glutinata* (with bulla), *Pulleniatina obliquiloculata* (with cortex) and *Cibicides mabahethi*) and their use for future paleoceanographic reconstructions.

Using a combination of spot Secondary Ion Mass Spectrometer, Electron Probe Micro-Analyzer and Scanning Electron Microscope image data, it is evident that authigenic overgrowths are present on both the external and internal test (shell) surfaces, yet the degree down-core as well as the associated bias is shown to be variable across the investigated species and proxies. Given the elevated authigenic overgrowth Mg/Ca (~12–22 mmol/mol) and $\delta^{18}O$ values (closer to the benthic isotopic compositions) the whole-test planktonic *G. ruber* (w) geochemical records are notably impacted beyond ~627.4 ka (24.7 mcd). Yet, considering the setting (i.e. bottom water location) for overgrowth formation, the benthic foraminifera $\delta^{18}O$ record is markedly less impacted with only minor diagenetic alteration beyond ~790.0 ka (28.7 mcd). Even though only the top of the *G. ruber* (w) and *C. mabahethi* records (whole-test data) would be suitable for paleo-reconstructions of absolute values (i.e. sea surface temperature, salinity, seawater $\delta^{18}O$), the long-term cycles, while dampened, appear to be preserved. Furthermore, planktonic species with thicker-tests (i.e. *P.*

obliquiloculata (w/c)) might be better suited, in comparison to thinner-test counter-parts (i.e. *G. glutinata* (w/b), *G. ruber* (w)), for traditional whole-test geochemical studies in shallow, carbonate-rich environments. A thicker test equates to a smaller overall bias from the authigenic overgrowth. Overall, if the diagenetic impact is constrained, as done in this study, these types of diagenetically altered geochemical records can still significantly contribute to studies relating to past tropical seawater temperatures, latitudinal scale ocean current shifts and South Asian Monsoon dynamics.

1. INTRODUCTION

In comparison to deep-sea records, high-resolution (both temporal and analytical) paleoclimate reconstructions for shallow-intermediate, equatorial regions are limited. This is in part due to (i) the drive to reconstruct and model past global ocean circulation patterns, which predominantly use high-temporally resolved deep-sea archives, and which are difficult to recover from lower latitudes and (ii) the increased susceptibility of calcifying organisms to diagenetic overprint in shallow, carbonate-rich environments. The tropics are an integral component of both regional and global climatic systems due to their heat and moisture storage capabilities (Gupta et al., 2010 and references within; Hastenrath et al., 1993; Schott et al., 2009). Yet, notably there is a lack of reliable sea surface temperature (SST) and $\delta^{18}O$ records from these equatorial regions, particularly from past extreme warming periods, which would further facilitate the understanding of tropical climatic systems. In this regard, we present a new high-resolution (analytical) tropical record from the Inner Sea of the Maldives archipelago in the equatorial Indian Ocean. We test the suitability of this unique tropical record for paleo-reconstructions given its shallow location, proximity to carbonate banks and the anticipated diagenetic alteration down-core.

Innumerable studies have shown that the geochemistry of foraminiferal tests (shells) are invaluable paleoceanographic, -climatic and -ecological archives (e.g. Birch et al., 2013; Kroon and Ganssen, 1989; Lisiecki and Raymo, 2005; Groeneveld et al., 2008; Raddatz et al., 2017; Stainbank et al., 2019). Yet, many of these geochemical proxies (e.g. Mg/Ca and $\delta^{18}O$) are susceptible to diagenetic alteration, which calls into question their fidelity (Edgar et al., 2015, 2013; Groeneveld et al., 2008; Panieri et al., 2017). According to Edgar et al. (2015) the foraminifera test wall, texture and morphology are prone to at least three diagenetic processes: overgrowth, partial dissolution and recrystallization. All three have the potential to bias the

109 original test geochemistry and affect the accuracy of paleo-reconstructions. As such, prior to
110 undertaking paleo-reconstructions, it is paramount to establish the diagenetic state of this
111 foraminiferal calcite. This is particularly important within carbonate-rich environments which
112 have high sediment porosity and permeability and thus a higher "diagenetic potential" in
113 comparison to the more impermeable clay-rich sediments (Edgar et al., 2013). Additionally,
114 in comparison to the more robust, heavily calcified benthic foraminifera, planktonic tests are
115 more susceptible to alteration (Edgar et al., 2013). Moreover, as there is a large array of
116 planktonic foraminifera test wall textures; this influence is not necessarily uniform between
117 species. Bé (1977) correlated increased diagenetic resistance for species with smaller pores,
118 thicker walls and larger test size. These considerations are important to aid in the selection of
119 less diagenetically predisposed foraminiferal species, particularly for depth stratified (i.e.
120 studies assessing discrete living and calcification depths within the water column) thermocline
121 reconstructions.
122
123 To contribute to an improved understanding of ocean-atmospheric interactions within the
124 tropical Indian Ocean, and the associated foraminiferal diagenetic processes, we present high
125 analytically resolved foraminiferal datasets from the shallow, Maldives Inner Sea.
126 Specifically, our study addresses the following issues: (i) the overall preservation state of the
127 individual long-term geochemical records and their suitability for future paleoceanographic
128 interpretations and (ii) the differential susceptibility to diagenesis for three planktonic
129 foraminiferal species, with discrete wall textures, and a benthic counterpart using a
130 combination of imaging and elemental/isotopic geochemical approaches.
131
132 **2. METHODS**

This study uses samples retrieved during the International Ocean Discovery Program (IODP) Expedition 359 in 2015. All samples come from Site U1467 (4°51.0274′N, 73°17.0223′E) drilled at a water depth of 487 m within the drift deposits of the Inner Sea of the Maldives archipelago in the northern equatorial Indian Ocean (Fig. 1) (Betzler et al., 2017). The base of these drift deposits have been biostratigraphically dated to 12.9-13.0 Ma, coinciding with the establishment of the South Asian Monsoon (Betzler et al., 2018, 2016). As such, the drift deposits represent an important paleoceanographic and -monsoon archive due to their unique ability to preserve continuous sediment records by bottom current deposition (Lüdmann et al., 2013). The top 61 meters composite depth (mcd) from Hole U1467B, C, composed of unlithified foraminifer-rich wackestone to packstone, were used in this study. The shipboard splice was adjusted after the Expedition based on X-ray fluorescence core scanner data using Fe intensity (counts per second, cps) (Kunkelova et al., 2018).

Fig. 1. Study location and position of IODP Expedition 359 Site U1467 in the Inner Sea of the Maldives (blue circle), located in the northern equatorial Indian Ocean (GEBCO Compilation Group, 2019).

Long-term, high-resolution (analytical) whole-test (whole-shell) stable isotopic ($\delta^{18}O$) records are compiled for three planktonic species, *Globigerinoides ruber* (white), *Globigerinita glutinata* (with bulla), *Pulleniatina obliquiloculata* (with cortex) and one benthic representative *Cibicides mabahethi*. In a few cases when the target benthic species is rare, *Cibicides wuellerstorfi* tests are included to ensure enough calcite for the isotopic measurements. Complementary whole-test Mg/Ca ratios are measured for *G. ruber* (w).

A combination of methods is utilized to constrain the influence and susceptibility of diagenetic alteration on the foraminiferal test geochemistry. A visual Scanning Electron Microscope (SEM) check is implemented, on selected samples, for both the target planktonic and benthic species. This visual check is then used to define a qualitative Diagenesis Rank (DR) to ascertain and track the down-core change in the preservation state of the foraminiferal tests. Supplementary spot-geochemical (isotopic and elemental) measurements are obtained using a Secondary Ion Mass Spectrometer (SIMS) and Electron Probe Micro-Analyzer (EPMA).

2.1. Site U1467 mineralogy and geochemistry

Site U1467 sediment core interstitial water chemistry and sediment mineralogy are presented in Betzler et al. (2017). Concentrations of Ca^{2+}, Mg^{2+} and Sr^{2+} were measured from interstitial water (IW) samples either by shipboard Inductively Coupled Plasma Atomic Emission Spectroscopy (ICP-AES) or shore-based ion chromatography (see Betzler et al., 2017; Blättler et al., 2019 for further details). Relative concentrations of aragonite, high-Mg calcite (HMC), low-Mg calcite (LMC), dolomite, and quartz were measured using X-ray powder diffraction (XRD) (see Betzler et al., 2017 for a full overview of the data collection methods). For simplicity we show only the data, reported as mbsf (meters below seafloor), from Hole U1467B as it yielded the most extensive and intact records at this site (Fig. 2).

Fig. 2. IODP Expedition 359 Hole U1467B sediment mineralogy and pore water geochemistry (Betzler et al., 2017).

2.2. Species selection criteria

To explore the susceptibility of different species to diagenetic alteration and the biases on their respective whole-test geochemical compositions, we assess three shallow/intermediate dwelling planktonic foraminiferal species: *G. ruber* (w), *G. glutinata* (w/b) and *P. obliquiloculata* (w/c). These species have reported apparent calcification depths for the northern equatorial Indian Ocean of ~70 m, 81 m and 74–104 m, respectively (Stainbank et al., 2019) and have discrete wall textures, thicknesses and porosities (Supplementary Material 1). *Globigerinoides ruber* (w) is chosen as it is the predominant foraminiferal species used for surface/near-surface seawater reconstructions (e.g. Birch et al., 2013; Bunzel et al., 2017; Rebotim et al., 2017; Stainbank et al., 2019). *Globigerinoides ruber* (w) is a spinose, shallow-dweller with a cancellate wall texture and a porosity of ~5 pores/25 x 25 μm (Bé, 1968) (Supplementary Material 1). *Globigerinita glutinata* (w/b) is included as a second shallow-dweller, as it is non-spinose with a smooth, microperforate wall texture with a porosity of ~112 pores/25 x 25 μm (Bé, 1968; Birch et al., 2013; Stainbank et al., 2019) (Supplementary Material 1). Lastly, the shallow-intermediate dweller *P. obliquiloculata* (w/c) is included as it is non-spinose, with a smooth wall texture (Birch et al., 2013; Stainbank et al., 2019). While the original test has a porosity of ~9 pores/25 x 25 μm, the formation of the smooth, glossy cortex layer drastically reduces the diameter and spherical nature of the pores resulting in a reduction in the overall porosity (Bé, 1968; Steinhardt et al., 2015) (Supplementary Material 1). *Cibicides mabahethi*, a calcareous hyaline epibenthic species, is chosen as the benthic representative for this site as it has been shown to accurately record bottom water conditions for the first ~200 kyr (time interval of the study by Bunzel et al., 2017) for the Maldives Inner Sea (Bunzel et al., 2017).

2.3. Traditional whole-test foraminiferal geochemical analysis

Sediment samples were air dried, weighed and washed through a 32 μm sieve to remove the finer silts and clay fraction. They were then oven-dried at 30°C for 48 hours, weighed and dry sieved into discrete fractions for foraminiferal picking. For all geochemical analyses, species were picked from pre-defined, narrow sieve size fractions, to minimize intra-specific ontogenetic isotopic fractionation effects (Stainbank et al., 2019). Additionally, to remove any adhering particles, and to prevent carbonate contamination, all picked specimens were precleaned in Milli-Q water for a few seconds by ultrasonication.

In total, 3802 traditional whole-test stable oxygen isotopic ($\delta^{18}O$) measurements were made (data is available on Pangaea). From 0–61 mcd a measurement for *G. ruber* (w: 212–250 μm) was obtained every ~3 cm. Isotopic analyses of *G. glutinata* (w/b: 125–150 μm) and *P. obliquiloculata* (w/c: 355–400 μm), were carried out across three selected intervals with differential diagenetic influences (see Section 3.2 for more details) at a resolution of 3-12 cm; Interval 1 (15.2–20.5 mcd), Interval 2 (31.4–34. 5 mcd) and Interval 3 (53.3–56.1 mcd). Benthic isotopic data (*C. mabahethi* > 180 μm) were only generated at a ~3 cm resolution between 0–40.0 mcd as below this interval they become scarce. The *G. ruber* (w) and *C. mabahethi* $\delta^{18}O$ measurements for the top 6.7 mcd (n = 441) were analyzed at Rutgers University on a MicroMass (FISONS) Optima Isotope Ratio Mass Spectrometer with an attached multi-prep device. Samples were reacted with 100 % phosphoric acid (H_3PO_4) at 90°C for 15 min, and the evolved CO_2 gas collected in a liquid nitrogen coldfinger and analyzed compared to a reference gas. The samples are corrected using an internal laboratory standard (RGF1), which is routinely run against NBS-19 and NBS-18. All other $\delta^{18}O$ data (n = 3361) were obtained at the Grant Institute of the University of Edinburgh on a Thermo Electron Delta+ Advantage Mass Spectrometer integrated with a Kiel carbonate III automated extraction line and corrected using the laboratory's internal standard. Approximately 0.05 mg

was required for each measurement with each expressed as parts per mil (‰) relative to Vienna Pee Dee Belemnite (VPDB). Replicate measurements of the standards give the instruments an analytical precision (1σ) of ~0.05 ‰ for $\delta^{18}O$ and $\delta^{13}C$. The reproducibility, based on inter-laboratory replicate measurements (n = 6), was ~0.20 ‰.

Mg/Ca ratios were measured on 30 pooled *G. ruber* (w: 212–250 μm) tests from a sample every ~3 cm, for the interval 14.8–31.4 mcd (n = 535; data is available on Pangaea). All samples were cleaned according to the standard oxidative protocol of Barker et al. (2003). Samples were then leached with a very weak 0.001N HNO_3 acid solution prior to dissolving in 0.075M HNO_3. The reductive cleaning step was excluded as it has been shown to cause the dissolution of the foraminiferal tests resulting in subsequently lower Mg/Ca values (Barker et al., 2003; Elderfield et al., 2006). Analyses were conducted at the Institute of Geosciences of the Goethe University of Frankfurt and at the School of GeoSciences at the University of Edinburgh. The former measurements (n = 232) were carried out by Inductively Coupled Plasma Optical Emission Spectrometry (ICP-OES) on a Thermoscientific iCap 6300 (dual viewing) and the latter (n = 303) on a Vista Pro ICP-OES. Inter-laboratory replicates (n = 11) were run to assess potential differences and the reproducibility which was determined to be better than 0.30 mmol/mol (mean difference). In Frankfurt, the final centrifuged sample solutions were diluted with an yttrium solution (1 mg/l) prior to measurement to allow for the correction of matrix effects. Whereas, in Edinburgh a set of six standard solutions (with increasing Ca concentrations from 0 to 100 %) were used for matrix and background correction (Sadekov et al., 2013). At both facilities, five calibration solutions were measured before each analysis to allow for intensity ratio calibrations. Element/Ca measurements were standardized using an internal consistency standard (ECRM 752-1, 3.761 mmol/mol Mg/Ca). Replicates of the ECRM at the Edinburgh (n = 61) and Frankfurt (n = 45) facilities yielded 2σ

Mg/Ca uncertainties (SD) of 0.15 and 0.17 mmol/mol, respectively. During all Mg/Ca measurements, the elements Al, Fe, and Mn were screened to check for Mn-Fe oxide coatings and clay mineral contamination. Procedural blanks were routinely run to monitor for potential contamination during the cleaning process.

2.4. Electron Probe Micro-Analyzer (EPMA) analysis

Samples for both EPMA and SIMS (Section 2.5) analyses were selected to provide representatives from the entire length of core including altered versus non-altered portions (see Section 3.2 for sample locations). Polished cross-sections of *G. ruber* (w) (n = 36) and *P. obliquiloculata* (w/c) (n = 6) tests were prepared by embedding the tests in Struers Epothin. Briefly, selected tests were (i) cleaned according to the same oxidative protocol (Barker et al., 2003) as for the traditional whole-test Mg/Ca geochemical analyses and (ii) placed umbilical side-down on adhesive film within 1-inch Struers mounting cups, then (iii) embedded in Epothin and degassed under high vacuum for 5 minutes and once set (iv) polished using a successively finer Struers water-based diamond suspension from 9 µm down to 0.25 µm to expose a cross-section of each test (Supplementary Material 2). All EPMA samples were then coated in 5 nm of carbon.

Quantitative Mg and Ca spot analyses and semi-quantitative elemental maps were measured using a JEOL JXA-8530F Electron Probe Micro-Analyzer, equipped with a Schottky field emission gun, at the Faculty of Geosciences and Environment of the University of Lausanne. Calcite, $CaCO_3$ (Ca = 39.98 wt%) and dolomite, $CaMg(CO_3)_2$ (Mg = 13.18 wt%) were used as standards for Ca and Mg, respectively. Spot measurements were acquired using a 10 kV accelerating voltage and probe size of 1–2 µm. Overview elemental maps were carried out with a 0.50 µm step size, an image resolution of 720 × 600 pixels, 7 kV accelerating voltage,

an electron beam current of 10 nA and a dwell time of 50 ms. Additional higher resolution elemental maps were obtained with a 0.23–0.29 μm step size and an image resolution of 256×192 pixels.

2.5. Secondary Ion Mass Spectrometer (SIMS) analysis

Polished cross sections, of selected *G. ruber* individuals (n = 27) were prepared for SIMS analyses following the same protocol as for the EPMA samples (Section 2.4), with the exclusion of the initial oxidative cleaning step. *In situ* oxygen isotope analyses were carried out using a Cameca IMS 1280-HR Secondary Ion Mass Spectrometer (SIMS) at the SwissSIMS ion probe facility within the University of Lausanne (Supplementary Material 3). A primary Cs+ ion beam with an intensity of 1.2nA was focused to a size of ~10 μm. The secondary ^{16}O and ^{18}O were detected simultaneously on two faraday cups, which were calibrated at the beginning of the session. The mass resolving power was set to 2400 (entrance slit set at 121 μm and multicollection slit 1), in order to fully remove possible ^{17}OH interference on mass 18. A single analysis took ~4 min, including 30 sec. of pre-sputtering, automatic centering of secondary deflectors and 20 cycles of 5 sec. of measurements. Calibration was made using an in-house pure calcite standard (UNIL-C1). Six analyses of the standard were made at the beginning of the measurements for each mount, after which UNIL-C1 was measured once every four analyses. Reproducibility of the standard (spot to spot) was 0.4 and 0.3 ‰ (2σ) on the two mounts, respectively. Internal uncertainty (single analysis) was 0.3 to 0.4 ‰ (2σ).

2.6. Scanning Electron Microscopy (SEM)

Thirty-five samples from the top 61 mcd of the core are used to constrain the preservation state of the target planktonic and benthic foraminiferal species. Samples are positioned at

regular intervals down-core and include representatives from glacial and interglacial peaks (see Section 3.2 for sample locations). From each sample, three to four *G. ruber* (w), *G. glutinata* (w/b), *P. obliquiloculata* (w/c) and *C. mabahethi/wuellerstorfi* tests were picked from the same size fractions as used for the geochemical analyses. Tests were cleaned for a few seconds by ultrasonication in Milli-Q water, cracked open and mounted on carbon based adhesive discs on standard SEM stubs. Stubs were coated, under vacuum, in 40 nm of gold using a Bal-tec SCD 050 sputter coater and imaged on a Thermo Fisher SEM FEIXL30SFEG. The preservation state of each species for each sample is ascertained, using SEM images, according to three categories (i) external test surface, (ii) internal test surface and (iii) test wall texture (Table 1). A ranking is assigned for each category and the sum (total out of 7) used to define the overall qualitative Diagenesis Rank (DR) for each species, with 0 defining 'pristine tests' and 7 the most 'diagenetically altered'.

Table 1. Diagenesis Rank categories and classifications.

Ranking	Category		
	1. External surface	**2. Internal surface**	**3. Wall texture**
0	Pristine unaltered surface texture with no authigenic overgrowth crystals present both on the test surface or within the pores		Pristine microgranular wall texture with well-defined pores
1	Small overgrowths present (up to ~0.5 μm) with a patchy-uniform distribution		Visibly altered wall texture with authigenic crystals within the wall cross sections either due to overgrowth precipitation or partial recrystallization
2	Mostly medium sized overgrowths present (~0.5-2 μm) with a uniform distribution		
3	Mostly large sized overgrowths present (>2 μm) with a uniform distribution		

Using the MATLAB v2018a software, a color-map is generated for each species to visualize the down-core evolution in preservation state (i.e. the change in DR). The 35 samples are used to define an initial matrix, and the rankings interpolated between each point using a linear function.

2.7. Age model

The stratigraphic framework for the upper 61 mcd of Site U1467 is established by graphically correlating both our planktonic *G. ruber* (w) and benthic *C. mabahethi* $\delta^{18}O$ records to the stacked reference curve of Ahn et al. (2017) (Prob-stack). Prob-stack was selected as it is based on a compilation of 180 global benthic isotope records and includes the datasets from the frequently used LR04 $\delta^{18}O$ stack of Lisiecki and Raymo (2005). The age model for our datasets is obtained using Analyseries v2.0.4 (Paillard et al., 1996). To facilitate the tuning process, initially all datasets were linearly detrended and our planktonic and benthic records smoothed (3 pt. running average) to eliminate some of the noise. The main glacial and interglacial peaks are used as the initial tie-points, with additional prominent maxima and minima subsequently correlated to optimize the visual alignment of the datasets (Supplementary Material 4).

3. RESULTS

3.1. Carbonate mineralogy

At IODP Expedition 359 Hole U1467B, LMC is ubiquitous, generally contributed by planktonic foraminifera and coccoliths, making up the bulk of the sediment mineralogy from the core-top down to 700 mbsf (Fig. 2, Betzler et al., 2017). Aragonite is contributed mainly by *Halimeda* fragments, coral fragments and pteropods, and decreases from ~46 % between 0–10 mbsf to only 9 % at 200 mbsf. From 200 to 500 mbsf aragonite still has a small, variable contribution (0–9 %). However, a marked increase in the aragonite contribution is noted from 500–600 mbsf (up to 23 %) with again a decrease down to 700 mbsf. HMC (with Mg^{2+} concentrations >4 mol%; Morse, 2003), which is contributed predominantly by red coralline algae, benthic foraminifera, bryozoans, and echinoderms, is only present (4–7 %) in the

sediments in the top 10 mbsf. Minor peaks in dolomite mainly occur within the top 400 mbsf. The pore-fluid species (Ca^{2+}, Mg^{2+} and Sr^{2+}) are visibly correlated with the aragonite concentrations (Betzler et al., 2017). Both Ca^{2+} and Mg^{2+} respectively, increase and decrease concomitantly with a reduction in aragonite percent contribution. Sr^{2+} increases rapidly to peak concentrations around 100 mbsf where it plateaus until ~500 mbsf below which there is a gradual decline.

The study interval (0 to ~61 mbsf), corresponds to Unit I (0–110 mbsf) of the logged lithostratigraphic units (a total of 6 units were identified) at Site U1467 (Betzler et al., 2017). It consists of an unlithified foraminifer-rich wackestone to packstone (very fine to fine grained) with a calcareous ooze matrix (Betzler et al., 2017). As noted, the abundance of aragonite is high in the study interval with HMC present in the first 10 mbsf. The species Ca^{2+} and Sr^{2+} are present in their lowest concentrations (mean Ca^{2+}: 10.61 mM, Sr^{2+} 111.42 mM) whereas, Mg^{2+} is in its highest concentration (mean Mg^{2+}: 53.58 mM) (Betzler et al., 2017).

3.2. Traditional whole-test foraminiferal geochemistry and Diagenesis Ranks

All geochemical records ($\delta^{18}O$ and Mg/Ca) show clear cyclicity down-core (Figs. 3-4). Based on the alignment of the stable isotope stratigraphies, the planktonic $\delta^{18}O$ *G. ruber* (w) record from 0–61.0 mcd represents the time interval 0–1800.0 kyr covering Marine Isotope Stage (MIS) 1-64 (Figs. 3a, 4a-b). The benthic record, spanning 0–40.0 mcd, encompasses the interval 0 to 1179.0 kyr (Figs. 3c, 4a,c), MIS1-35. The sedimentation rate varies down-core between 0.4–16.3 cm/kyr (Fig. 4d).

Fig. 3. Long-term geochemical records from IODP Expedition 359 Site U1467 against core depth with (a) the *G. ruber* (w) $\delta^{18}O$, (b) Mg/Ca records and (c) the *C. mabahethi*

$\delta^{18}O$ record. Visual SEM check (grey circles) and EPMA/SIMS (red and black circles, respectively) samples are shown for reference. A 3-pt moving average smoothing was applied to our datasets (thick lines) to highlight the cycles.

Fig. 4. (a) The benthic foraminifera $\delta^{18}O$ stack (prob-stack) of Ahn et al. (2017) **is used to obtain the age model for (b) IODP Expedition 359 Site U1467 *G. ruber* (w) and (c) *C. mabahethi* $\delta^{18}O$ records. A 3-pt moving average smoothing was applied to our datasets (b, c: thick lines) to highlight the cycles. Sedimentation rates (Sed. Rate) are referenced as cm/kyr in (d). Marine Isotope Stages (MIS) are shown (vertical dashed lines) and form the main tie-points for the age model (Supplementary Material 4).**

SEM observations reveal diagenetic alterations are primarily due to the precipitation of authigenic calcite (overgrowth) (Fig. 5). Furthermore, the diagenetic susceptibility of the four investigated species, *G. ruber* (w), *G. glutinata* (w/b), *P. obliquiloculata* (w/c) and *C. mabahethi,* differs down-core (Figs. 5-6). The resultant Diagenesis Rank (DR) values reflect a gradual decline, in the overall preservation state from 0 to 1800.0 kyr (0–61.0 mcd) (sample locations noted on Figs. 3, 6). While this down-core decline is variable across all species, all have pristine, unaltered tests in the core-top samples (359-U1467A, B-Mudline) (Fig. 5). Further down-core, authigenic overgrowths occur both on the internal and external test surfaces and within pores, resulting in a reduction in pore-size until complete infilling is achieved (Fig. 5, Supplementary Material 1). The size of these authigenic overgrowths varies from small and patchy to large (> 2 μm) well-developed, euhedral crystals growing perpendicular to the test wall and covering the entire inner and outer test surfaces (Supplementary Material 1).

Fig. 5. Scanning Electron Microscope (SEM) images of (a) *G. ruber* (w), (b) *G. glutinata* (w/b), (c) *P. obliquiloculata* (w/c) and (d) *C. mabahethi/C. wuellerstorfi* showing the outer (1, 2 and 4) and inner test surfaces (3, 5). Images of pristine IODP Expedition 359 Site U1467 tests from the core-top (Sample at 0 ka: A, B-Mudline) are shown in 1-3 and images of diagenetically altered tests (Sample at 1743.8 ka, 58.7 mcd: B-7H-3, 75-76 cm) are shown in 4-5. Representative examples of overgrowth size and distribution are shown for the inner test surfaces of *G. ruber* (w) in (e-h) (Samples: e. B-Mudline; f. B-3H-4, 99-100 cm; g. B-4H-5, 36-37 cm; h. C-6H-5, 57-58 cm). White bars show test wall thicknesses and red arrows indicate representative examples of overgrowth crystals. Whole-test scale bars = 100 µm and close-up image scale bars = 20 µm.

Fig. 6. Long-term stable isotope ($\delta^{18}O$) records for IODP Expedition 359 Site U1467 for (a) the planktonic species *G. ruber* (w) with intervals 1-3 comparing *G. glutinata* (w/b) and *P. obliquiloculata* (w/c) records (note: Selected Marine Isotope Stages (MIS) are shown for reference); Diagenesis Rank (DR) color maps are shown for (b) *G. ruber* (w), (c) *G. glutinata* (w/b), (d) *P. obliquiloculata* (w/c) and (e) *C. mabahethi* with (f) the long-term $\delta^{18}O$ record for the benthic species *C. mabahethi*. The samples used for the visual SEM check are also shown as grey circles on (a). Red and teal curves show $\delta^{18}O$ *G. ruber* (w) and *C. mabahethi* data, respectively from Bunzel et al. (2017)**. A 3-pt moving average smoothing was applied to the datasets (thick lines) to highlight the cycles.**

Pulleniatina obliquiloculata (w/c) appears to be the most susceptible species to authigenic overgrowth with medium sized, well-developed crystals already observed at ~274.5 ka (11.6 mcd) on the external test surfaces. In contrast, these are first observed on *G. ruber* (w) at ~790.0 ka (28.7 mcd), *G. glutinata* (w/b) at ~558.3 ka (22.2 mcd) and the benthic tests further

down core at ~807.9 ka (29.1 mcd). Large well-developed authigenic crystals are evident on tests of *G. ruber* (w), *G. glutinata* (w/b), *P. obliquiloculata* (w/c) and *C. mabahethi* from ~1190.9 ka (40.6 mcd), ~1015.1 ka (36.0 mcd), ~864.7 ka (31.3 mcd) and ~872.0 ka (31.7), respectively (Supplementary Material 1). In addition to size, differences in overgrowth distributions are noted between the planktonic and benthic species. While all species show roughly similar development of overgrowth crystals across their outer test surface, with concentrations of overgrowths in the pores, distinct differences are observed on their inner test surfaces. For the planktonic species, authigenic overgrowths are more or less homogeneous across the surface whereas for the benthic species, they are generally concentrated within the pores and along the sutures with patchy growth across the inner surfaces (Supplementary Material 1).

Intervals 1-3 were specifically selected, with reference to the *G. ruber* (w) DR data, as representative segments with differential diagenetic influences. Variability between the three planktonic $\delta^{18}O$ records does occur across the intervals (Fig. 6). Interval 1, which covers MIS10-13 (354.0–505.0 kyr), has the lowest DR values for all species (0–3). Interval 2, which covers MIS21-26 (866.7–974.0 kyr), is located in the section with a notable increase in the respective DR values (2–4). Finally, Interval 3 covers MIS54-59 (1573.8–1690.9 kyr) in the most altered portion of the records with the highest DR values (> 4). The glacial-interglacial cycles are more prominent across all records in Interval 1. Both *G. ruber* (w) and *P. obliquiloculata* (w/c) display a large amplitude change from the glacial peak MIS12 across the deglaciation to the interglacial peak MIS11 (Δ ~2.20 ‰ and 2.50 ‰, respectively). *Globigerinita glutinata* (w/b) shows a smaller change across MIS12 to MIS11 (Δ 1.41 ‰), and less prominent glacial-interglacial peaks in Interval 2 compared to *G. ruber* (w) and *P. obliquiloculata* (w/c). Interval 3 shows notably higher isotopic values with the glacial-

449 interglacial peaks markedly reduced, although still clearly visible, for all species. Despite the
450 variation and extent of diagenetic alteration, Pleistocene glacial-interglacial cycles can be
451 readily identified in all long-term $\delta^{18}O$ records (Fig. 6). However, beyond ~1300 ka (46.1
452 mcd), the *G. ruber* (w) data shows a notable down-core trend towards higher $\delta^{18}O$ values (Fig.
453 6).
454
455 **3.3. Comparison of biogenic calcite and authigenic overgrowth geochemistry**
456 SIMS spot analyses (~10 μm diameter) are similar to the *G. ruber* (w) test wall thickness (~9–
457 12 μm) such that a large proportion of the measurements partly overlapped onto epoxy. The
458 location of these compromised analyses (n = 35) was confirmed by SEM observation, and
459 only those measurements which were located solely on the foraminifera test were included in
460 the reported analyses (Fig. 7, Supplementary Material 3). Overall, 16 SIMS and 36 EPMA
461 spot measurements from the F-0 (final), F-1 (penultimate) and F-2 (antepenultimate)
462 chambers were measured on seven samples for *G. ruber* (w), (Fig. 7, Supplementary
463 Materials 2-3). An additional five EPMA spot analyses of large authigenic overgrowths were
464 measured (Fig. 7, Supplementary Material 2). Limited SIMS and EPMA sample sets were
465 obtained due to the limitations of spot size (for SIMS) and epoxy stability (for EPMA). Yet,
466 the datasets are still deemed sufficient to assess overall trends and the application of these
467 micro-analytical techniques in foraminiferal diagenetic studies. Mean values and standard
468 deviations of the measurements along with sample locations (with reference on the $\delta^{18}O$ *G.*
469 *ruber* (w) curve) are shown in Figure 7.
470
471 **Fig. 7. (a) SIMS and (b) EPMA spot data versus whole-test ICP-MS/ICP-OES**
472 **measurements for *G. ruber* (w) with the location of the samples (circles with number ID:**
473 **black = SIMS and red = EPMA samples) referenced on (c) the long-term *G. ruber* (w)**

$\delta^{18}O$ curve; (d) *G. ruber* (w) whole-test Mg/Ca data and (e) the *G. ruber* (w) Diagenesis Rank (DR) color map. IODP Expedition 359 Site U1467 sample IDs: (1) A, B-Mudline; (2) B-3H-3, 9-10 cm; (3) B-4H-5, 36-37 cm; (4) B-6H-2, 75-76 cm; (5) B-6H-3, 75-76 cm; (6) B-6H-4, 75-76 cm; (7) B-7H-3, 75-76 cm. Sea surface temperature (SST) calculations are based on the *G. ruber* (w) equation of Anand et al. (2003)**. Red curve shows $\delta^{18}O$ *G. ruber* (w) data from** Bunzel et al. (2017). **A 3-pt moving average smoothing was applied to all datasets (thick lines) to highlight the cycles. Note: F-0 (final), F-1 (penultimate) and F-2 (antepenultimate) chambers, WT= whole-test and OG = overgrowth measurements. WT data in a) and b) for A, B-Mudline Sample 1 is from Stainbank et al. (2019).**

Whole-test $\delta^{18}O$ and Mg/Ca values are comparable to SIMS and EPMA spot measurements for core-top Sample 1 at 0 ka (0 mcd) and to EPMA data for Sample 2 at 409.0 ka (17.4 mcd). From Sample 3 (= 864.7 ka, 31.3 mcd) to Sample 7 (= 1743.8 ka, 58.7 mcd) the whole-test *G. ruber* geochemical values are consistently higher than the SIMS ($z = 1.5\text{-}5.2$; $p = 0.9\text{-}1$) and EPMA ($z = 2.7\text{-}8$; $p = 1$) data obtained from individual chambers (Fig. 7a-b). Moreover, the difference varies with the highest values and largest offsets in the deepest, oldest sample. Interestingly, one F-1 SIMS data point for Sample 7 hit substantial diagenetic overgrowths and has a relatively high $\delta^{18}O$ value of -1.24 ‰ (Supplementary Material 3). The EPMA overgrowth data (Samples 6 and 7) reveals a HMC composition with 3–6 times higher Mg/Ca values than original test compositions. Samples 3–7 cover the interval corresponding to an observed change in the slope of the long-term *G. ruber* (w) $\delta^{18}O$ record with a down-core trend towards higher values. A marked increase in the slope of the long-term *G. ruber* (w) Mg/Ca record is, however, already noted prior to Sample 3 (Fig. 7d). Similar to the EPMA spot analyses (Fig. 7b), the elemental maps of both *G. ruber* (w) and *P. obliquiloculata* (w/c)

499 show clear Mg enrichment in the authigenic overgrowths (Fig. 8). Both species have a LMC
500 test (Figs. 8.a1, 8.b1), whereas *P. obliquiloculata* (w/c) has natural HMC growth bands
501 indicated on Figure 8 (yellow arrows). Overgrowths, on both the inner and outer test surfaces,
502 have 4–10 times higher Mg intensities than the biogenic calcite (Figs. 8.a2, 8.b2).
503
504 **Fig. 8. Mg (intensity) EPMA maps. Examples of IODP Expedition 359 Hole U1467B**
505 **pristine specimens (Mudline) are shown for (a1) *G. ruber* (w) and (b1) *P. obliquiloculata***
506 **(w/c) with diagenetically altered examples shown for (a2) *G. ruber* (w) (7H-3, 75-76 cm)**
507 **and (b2) *P. obliquiloculata* (w/c) (6H-4, 75-76 cm). T = test, OG = overgrowth, EE = edge**
508 **effect. Reference to sample locations (ID1, 6 and 7) are shown on Fig. 7. Note the high-**
509 **Mg (yellow arrows) and low-Mg banding in the *P. obliquiloculata* (w/c) tests. Scale bars**
510 **= 10 µm.**
511
512 **4. DISCUSSION**
513 **4.1. Preservation state of the individual long-term geochemical records**
514 The stable oxygen isotope composition ($\delta^{18}O$) of the original foraminiferal test is a function of
515 the ambient seawater temperature and $\delta^{18}O$ composition during its initial precipitation
516 (Pearson, 2012). Similarly, biogenic test Mg/Ca ratios reflect ambient seawater temperatures
517 (e.g. Raddatz et al., 2017; Rippert et al., 2016). Authigenic overgrowth is anticipated to occur
518 near the sediment/bottom-water interface and down-core (e.g. Regenberg et al., 2007). As
519 such, its oxygen isotope composition is controlled by a variety of factors including
520 thermodynamic fractionation, the $\delta^{18}O$ and pH of the precipitating fluid as well as mineralogy
521 and kinetic effects during the precipitation (Kim and O'Neil, 1997; O'Neil et al., 1969; Swart,
522 2015). The elemental ratio compositions are related to site mineralogy and pore water
523 geochemistry.

From 0 to ~200 kyr (0 to ~7.3 mcd), the cycles and amplitudes of IODP Expedition 359 Site U1467 $\delta^{18}O$ *G. ruber* (w) and *C. mabahethi* records, are comparable to the records produced by Bunzel et al. (2017) (Fig. 6). Bunzel et al. (2017) compiled stable isotopic datasets from Core SO236-052-4 retrieved from the Maldives Inner Sea (03°55.09′N; 73°08.48′E) at a water depth of 382 m (Note: the slight amplitudinal difference between the benthic datasets is due to differences in study site depths). Notably, Bunzel et al. (2017) used a lower analytical resolution and a larger test size (250–350 μm) for their *G. ruber* (w) record, yet visually the two datasets are nearly identical. This attests to the good preservation state of Site U1467 samples for the first ~200 kyr (7.3 mcd). Furthermore, we can consider the *G. ruber* (w) $\delta^{18}O$ and Mg/Ca records from 0 to ~627.4 kyr (0 to ~24.7 mcd) to be pristine/near-pristine. This is reflected by the low DR values (0-2) and is manifest in the coherence between the SIMS and EPMA spot analyses data (Samples 1 and 2) and the whole-test geochemical datasets. In particular, EPMA data for Sample 2 (Fig. 7b) illustrates that at least up until 409.0 ka (17.4 mcd) the whole-test Mg/Ca values closely reflect the original test geochemistry. While small, patchy HMC overgrowth is present on the internal surfaces (DR = 1), it does not appear to be sufficient to bias the whole-test geochemistry. Calculated SSTs are also notable for being within the modern, seasonal seawater temperature range (Fig. 7d) (Krahmann and Krüger, 2018; Quadfasel, 2017; Reolid et al., 2017).

The degree of influence of the authigenic overgrowth on whole-test geochemical records can vary significantly and is not necessarily consistent across the various proxies (i.e. $\delta^{18}O$ versus Mg/Ca). A change in the preservation state of the *G. ruber* (w) tests occurs between ~627.4 to 790.0 kyr (24.7–28.7 mcd) onwards (DR values > 2). Discrepancies are also recorded by the SIMS and EPMA data from individual chambers which are significantly lower than respective

549 whole-test geochemical values from Sample 3 (Δ ~1.1 ‰ and ~1.5 mmol/mol, respectively) to
550 Sample 7 (Δ ~1.8 ‰ and ~4.1 mmol/mol, respectively) (Fig. 7a, b). There is a notable down-
551 core increase in the slope of the $\delta^{18}O$ *G. ruber* (w) record. This is captured by SIMS Samples
552 3–5, which show a ~1 ‰ increase in the whole-test values and Sample 7, the most
553 diagenetically altered, which shows a ~2 ‰ increase. The compositional trends observed in
554 the $\delta^{18}O$ data are notably amplified in the long-term Mg/Ca record, with a steeper down-core
555 slope increase. Considering the original test geochemistry is usually < 6 mmol/mol, only a
556 limited amount of HMC overgrowth (~12–22 mmol/mol) would be required to bias the
557 whole-test Mg/Ca towards significantly higher values (Fig. 7). This is reflected in EPMA
558 Sample 3 (= 864.7 ka, 31.3 mcd), which has minimal overgrowth present on the external test
559 surface (external category Diagenesis Rank = 1), yet small-medium well-developed euhedral
560 crystals across the entire inner test surface (internal category Diagenesis Rank = 2). This
561 overgrowth, although small, is sufficient to elevate the whole-test Mg/Ca values and increase
562 the SST reconstruction by ~2°C. This is further substantiated by EPMA Samples 4, 6 and 7,
563 which have higher DR values due to poorer preservation states and an increased presence
564 and/or size of overgrowth crystals. All have lower spot F-0 and F-1 chamber Mg/Ca values in
565 comparison to the whole-test data, resulting in progressively larger discrepancies in SST
566 estimates of ~4–7°C.
567
568 The precipitation of HMC overgrowths, as opposed to the more stable LMC, could be a
569 function of both the composition and content of the bulk sediment as well as the pore water
570 geochemistry (e.g. Panieri et al., 2017; Regenberg et al., 2007). At Site U1467, HMC is only
571 present in the top 10 mbsf (Fig. 2). Where HMC in the sediment has dissolved, Mg^{2+} is
572 released and may be incorporated (elsewhere) in crystalline overgrowths on biogenic
573 carbonates. Aragonite dissolution and active sulphate reduction were noted below 50 mbsf at

574 this site by Betzler et al. (2017). The former had been noted earlier in a pteropod study by
575 Sreevidya et al. (2019) who reported intense dissolution of aragonitic pteropods beyond ~800
576 ka. As such, an increased saturation state of pore waters, with respect to Mg^{2+}, in combination
577 with active sulphate reduction may have favored HMC over LMC authigenic precipitates
578 (Panieri et al., 2017; Swart, 2015). Higher resolution sediment mineralogy together with
579 petrography and pore water profiles are needed to conclude as to the exact processes behind
580 the depth occurrence and Mg-content of the HMC overgrowths. However, the combined
581 influence of HMC with naturally elevated $\delta^{18}O$ values (Tarutani et al., 1969), with
582 thermodynamic fraction (Δ ~19°C between the surface seawater and at 487 m depth) and
583 related fluid geochemistry changes would further justify the precipitation of authigenic
584 overgrowths with elevated $\delta^{18}O$ values. These processes could thus explain the notable biases
585 (stable isotopic and elemental) on the planktonic whole-test geochemical data from
586 SIMS/EPMA Sample 3 (= 864.7 ka, 31.3 mcd) to 7 (= 1743.8 ka, 58.7 mcd).
587
588 Although no SIMS or EPMA data was collected for the benthic *C. mabahethi* species, a
589 change in preservation state (DR > 2) occurs between ~790.0 to 807.9 kyr (28.7–29.1 mcd).
590 As such, we can surmise the records beyond this interval to have some degree of diagenetic
591 overprint (Figs. 6e-f). This is supported by observations of large, well-developed overgrowth
592 on the internal test surfaces at 872.0 ka (31.7 mcd). Even though minimal overgrowth is
593 present on the external surfaces, it is presumed that the large internal crystals would be
594 sufficient to affect the whole-test geochemical records. However, although the Mg/Ca biases
595 would be similar to that on the *G. ruber* (w) records, the $\delta^{18}O$ influences should be minor
596 considering diagenetic precipitation is anticipated to occur near the sediment/bottom water
597 interface in close proximity to where the original biogenic calcite precipitated (Edgar et al.,
598 2013). This would imply similar seawater temperatures; however, differences in pH,

599 mineralogy and kinetic effects during the authigenic overgrowth precipitation cannot be
600 excluded. This hypothesis is supported by the prominent glacial-interglacial cycles with their
601 amplitudes seemingly well preserved for the entirety of the benthic $\delta^{18}O$ record (0-1179.0 kyr)
602 (Figs. 3-4, 6).
603
604 **4.2. Diagenetic susceptibility of individual planktonic species**
605 We found distinct differences in the preservation state of the three investigated planktonic
606 species. As such, the diagenetic bias on their respective whole-test geochemical compositions
607 varies. This is illustrated in Intervals 1-3 in Figure 6, with a variable preservation of the
608 glacial-interglacial amplitudinal differences. The whole-test *G. ruber* (w), *G. glutinata* (w/b)
609 and *P. obliquiloculata* (w/c) $\delta^{18}O$ records all reflect clear, large amplitude cycles within
610 Interval 1. However, relative to the thicker-walled *P. obliquiloculata* (w/c), the former two
611 species record dampened signals with the peaks notably less pronounced across Interval 2.
612 Across Interval 3, in the most diagenetically altered portion of the record, all datasets are
613 notably affected with reduced glacial-interglacial maxima and minima and all $\delta^{18}O$ records
614 converge because of increasing whole test $\delta^{18}O$ values.
615
616 It might seem contradictory that the species, which appears to be most diagenetically
617 susceptible, would have the best whole-test geochemical preservation across Interval 2.
618 However, as *P. obliquiloculata* (w/c) has the thickest test (~24 μm, Figs. 5, 9), the rationale is
619 that a thicker test would equate to more of the whole-test composition being weighted by the
620 biogenic calcite. Therefore, in proportion to the primary signal, the authigenic overgrowth
621 would contribute a smaller percentage and result in a smaller bias compared to *G. ruber* (w)
622 and *G. glutinata* (w/b) which have significantly thinner tests (~9–12 and ~6–10 μm,
623 respectively; Figs. 5, 9). This is in accordance with observations by Bé (1977) and Kucera

(2007). Bé (1977) correlated increased diagenetic resistance for species with smaller pores, thicker walls and larger test size, while Kucera (2007) reports an increase in dissolution resistance for species with a lower porosity (Fig. 9).

Fig. 9. Interpretations of diagenetic susceptibilities for the whole-test geochemistry of the three investigated planktonic species. Interpretations are based on Diagenesis Rank (DR) values, spot EPMA/SIMS and whole-test geochemistry data from IODP Expedition 359 Site U1467. Interpretations of dissolution susceptibilities after Kucera (2007).

5. CONCLUSIONS

Foraminiferal geochemical records from shallow, carbonate platforms are integral for understanding global paleoceanographic and -climatic trends but are subject to diagenetic influences. This is the case at IODP Expedition 359 Site U1467, which represents a shallow-intermediate water archive from the equatorial Indian Ocean of importance for South Asian Monsoon (SAM) climatic studies and latitudinal scale shifts of ocean currents. Prior to utilizing our high-analytically resolved geochemical records for paleo-reconstructions, it is important to constrain the influence of diagenetic alteration on both the preservation of the original geochemical compositions and long-term cyclicity.

The presence and influence of authigenic overgrowths on the inside and/or outside of the foraminiferal test as well as through the partial or full recrystallization of the test wall has long been recognised. Importantly, this authigenic calcite is not ubiquitous or uniform in terms of presence, size, distribution or geochemical composition and as such should be assessed on an individual study site basis. For simplicity, ease of use and to facilitate reproducibility in other studies, the qualitative DR detailed and used in this study only

649 constrains the presence of authigenic overgrowths on the test surfaces as well as within the
650 wall structure. However, it is noted that both the primary and authigenic calcite can be
651 susceptible to dissolution, which would further alter the geochemical compositions. These
652 dissolution features, which can include etched surfaces as well as lattice-like calcite
653 structures, as well as partial recrystallization of the wall texture are noted in the deepest,
654 oldest studied samples.
655
656 The degree of influence of the authigenic overgrowth on the whole-test geochemistry varies
657 across the foraminiferal species (*G. ruber* (w), *G. glutinata* (w/b), *P. obliquiloculata* (w/c), *C.*
658 *mabahethi*) and proxies (i.e. $\delta^{18}O$ versus Mg/Ca). Considering the site mineralogy, whole-test
659 Mg/Ca compositions are notably more impacted than $\delta^{18}O$ records. However, taking into
660 consideration our individual spot analyses (SIMS and EPMA) and DR data, the top ~627.4
661 kyr of the *G. ruber* (w) Mg/Ca and $\delta^{18}O$ records are well preserved and largely reflect the
662 primary geochemical compositions. Given the setting of overgrowth precipitation, the benthic
663 *C. mabahethi* $\delta^{18}O$ record from 0–790.0 kyr (DR = 0–2), if not the entire benthic record, is
664 considered to have pristine/near-pristine preservation of the primary $\delta^{18}O$ signal. As such, the
665 top portions of both the *G. ruber* (w) (0 to ~627.4 kyr; 0-24.7 mcd) and *C. mabahethi* (0 to
666 ~790.0 kyr; 0-28.7 mcd) records (whole-test data) are suitable for paleoceanographic
667 reconstructions of absolute seawater temperature, salinity and $\delta^{18}O$ values. Notwithstanding
668 the down-core diagenetic influences, the glacial-interglacial cyclicity, while dampened, is
669 maintained as attested by the coherence of both the *G. ruber* (w) and *C. mabahethi* $\delta^{18}O$
670 records with Prob-stack. As such, the complete geochemical records could still be used for
671 cyclostratigraphy to assess long-term orbital scale properties.
672

673 Overall, we show foraminiferal species (e.g. *P. obliquiloculata*) with thicker tests are better
674 suited for whole-test geochemical analyses, in diagenetically susceptible settings, as they have
675 a higher proportion of biogenic calcite relative to authigenic overgrowth. Moreover, while
676 only a portion of our whole-test geochemical records reflect the primary compositions, SIMS
677 and EPMA spot measurements can be utilized to overcome any biases in diagenetically
678 impacted intervals. Considering the importance of these types of records for tropical
679 temperature studies, it is vital to employ an approach, whether it be spot versus whole-test
680 analyses, the utilization of specimens with thicker tests or a visual DR, which will allow the
681 preservation state to be assessed to obtain more accurate and reliable paleo-reconstructions.
682

683 **6. ACKNOWLEDGEMENTS**

684 Funding: This work was funded by the Swiss National Science Foundation (SNSF) through
685 grant number 200021_165852/1 awarded to SSp. DK acknowledges funding support from the
686 Natural Environment Research Council (NERC) through grant number NERC-
687 NE/N012739/1. Additionally, EDB was funded through the SNSF project
688 QuantiCarb@Spring (project number: 154810).
689

690 The authors would like to thank the International Ocean Discovery Program (IODP) for
691 supplying the samples used in this study. From the University of Fribourg, we thank Alex
692 Salzmann for his help with embedding the EPMA and SIMS samples, Christoph Neururer for
693 his help with the SEM imaging and Sandra Borderie for her help with Figure 1, which was
694 drawn using the free software package GMT (The Generic Mapping Tools; Wessel and
695 Smith, 1991). Martin Robyr is thanked for his assistance during the EPMA analysis at the
696 University of Lausanne. FIERCE is financially supported by the Wilhelm and Else Heraeus
697 Foundation, which is gratefully acknowledged. This is FIERCE contribution No. 19. Lastly,

we acknowledge the constructive comments of two anonymous reviewers that helped to refine the manuscript.

REFERENCES

Ahn, S., Khider, D., Lisiecki, L.E., Lawrence, C.E., 2017. A probabilistic Pliocene–Pleistocene stack of benthic $\delta^{18}O$ using a profile hidden Markov model. Dyn. Stat. Clim. Syst. 2, 1–16. https://doi.org/10.1093/climsys/dzx002

Anand, P., Elderfield, H., Conte, M.H., 2003. Calibration of Mg/Ca thermometry in planktonic foraminifera from a sediment trap time series. Paleoceanography 18, 1050. https://doi.org/10.1029/2002PA000846

Barker, S., Greaves, M., Elderfield, H., 2003. A study of cleaning procedures used for foraminiferal Mg/Ca paleothermometry. Geochemistry, Geophys. Geosystems 4, 8407. https://doi.org/10.1029/2003GC000559

Bé, A.W.H., 1977. An ecological, zoogeographic and taxonomic review of recent planktonic foraminifera. Ocean. Micropaleontol. 1, 1–100.

Bé, A.W.H., 1968. Shell porosity of Recent planktonic foraminifera as a climatic index. Science (80-.). 161, 881–884.

Betzler, C., Eberli, G.P., Alvarez Zarikian, C.A., Alonso-García, M., Bialik, O.M., Blättler, C.L., Guo, J.A., Haffen, S., Horozal, S., Inoue, M., Jovane, L., Kroon, D., Lanci, L., Laya, J.C., Ling Hui Mee, A., Lüdmann, T., Nakakuni, M., Nath, B.N., Niino, K., Petruny, L.M., Pratiwi, S.D., Reijmer, J.J.G., Reolid, J., Slagle, A.L., Sloss, C.R., Su, X., Swart, P.K., Wright, J.D., Yao, Z., Young, J.R., 2017. Proceedings of the International Ocean Discovery Program Volume, 359. Coll. Station. TX (International Ocean Discov. Program). https://doi.org/10.14379/iodp.proc.359.102.2017

Betzler, C., Eberli, G.P., Kroon, D., Wright, J.D., Swart, P.K., Nath, B.N., Alvarez-Zarikian,

C.A., Alonso-García, M., Bialik, O.M., Blättler, C.L., Guo, J.A., Haffen, S., Horozal, S., Inoue, M., Jovane, L., Lanci, L., Laya, J.C., Ling Hui Mee, A., Lüdmann, T., Nakakuni, M., Niino, K., Petruny, L.M., Pratiwi, S.D., Reijmer, J.J.G., Reolid, J., Slagle, A.L., Sloss, C.R., Su, X., Yao, Z., Young, J.R., 2016. The abrupt onset of the modern South Asian Monsoon winds. Sci. Rep. 6, 29838. https://doi.org/10.1038/srep29838

Betzler, C., Eberli, G.P., Lüdmann, T., Reolid, J., Kroon, D., Reijmer, J.J.G., Swart, P.K., Wright, J., Young, J.R., Alvarez-Zarikian, C., Alonso-García, M., Bialik, O.M., Blättler, C.L., Guo, J.A., Haffen, S., Horozal, S., Inoue, M., Jovane, L., Lanci, L., Laya, J.C., Hui Mee, A.L., Nakakuni, M., Nath, B.N., Niino, K., Petruny, L.M., Pratiwi, S.D., Slagle, A.L., Sloss, C.R., Su, X., Yao, Z., 2018. Refinement of Miocene sea level and monsoon events from the sedimentary archive of the Maldives (Indian Ocean). Prog. Earth Planet. Sci. 5, 5. https://doi.org/10.1186/s40645-018-0165-x

Birch, H., Coxall, H.K., Pearson, P.N., Kroon, D., O'Regan, M., 2013. Planktonic foraminifera stable isotopes and water column structure: Disentangling ecological signals. Mar. Micropaleontol. 101, 127–145. https://doi.org/doi.org/10.1016/j.marmicro.2013.02.002

Blättler, C.L., Higgins, J.A., Swart, P.K., 2019. Advected glacial seawater preserved in the subsurface of the Maldives carbonate edifice. Geochim. Cosmochim. Acta 257, 80–95. https://doi.org/doi.org/10.1016/j.gca.2019.04.030

Bunzel, D., Schmiedl, G., Lindhorst, S., Mackensen, A., Reolid, J., Romahn, S., Betzler, C., 2017. A multi-proxy analysis of Late Quaternary ocean and climate variability for the Maldives, Inner Sea. Clim. Past 13, 1791–1813. https://doi.org/10.5194/cp-13-1791-2017

Detlef, H., Sosdian, S.M., Kender, S., Lear, C.H., Hall, I.R., 2020. Multi-elemental composition of authigenic carbonates in benthic foraminifera from the eastern Bering

748 Sea continental margin (International Ocean Discovery Program Site U1343). Geochim.
749 Cosmochim. Acta 268, 1–21. https://doi.org/10.1016/j.gca.2019.09.025
750 Edgar, K.M., Anagnostou, E., Pearson, P.N., Foster, G.L., 2015. Assessing the impact of
751 diagenesis on $\delta^{11}B$, $\delta^{13}C$, $\delta^{18}O$, Sr/Ca and B/Ca values in fossil planktic foraminiferal
752 calcite. Geochim. Cosmochim. Acta 166, 189–209.
753 https://doi.org/10.1016/j.gca.2015.06.018
754 Edgar, K.M., Pälike, H., Wilson, P.A., 2013. Testing the impact of diagenesis on the $\delta^{18}O$ and
755 $\delta^{13}C$ of benthic foraminiferal calcite from a sediment burial depth transect in the
756 equatorial Pacific. Paleoceanography 28, 468–480. https://doi.org/10.1002/palo.20045
757 Elderfield, H., Yu, J., Anand, P., Kiefer, T., Nyland, B., 2006. Calibrations for benthic
758 foraminiferal Mg/Ca paleothermometry and the carbonate ion hypothesis. Earth Planet.
759 Sci. Lett. 250, 633–649. https://doi.org/doi:10.1016/j.epsl.2006.07.041
760 GEBCO Compilation Group. 2019. GEBCO 2019 Grid. http://doi:10.5285/836f016a-33be-
761 6ddc-e053-6c86abc0788e
762 Groeneveld, J., Nürnberg, D., Tiedemann, R., Reichart, G.J., Steph, S., Reuning, L., Crudeli,
763 D., Mason, P., 2008. Foraminiferal Mg/Ca increase in the Caribbean during the Pliocene:
764 Western Atlantic Warm Pool formation, salinity influence, or diagenetic overprint?
765 Geochemistry, Geophys. Geosystems 9, Q01P23.
766 https://doi.org/10.1029/2006GC001564
767 Gupta, A.K., Sarkar, S., De, S., Clemens, S.C., Velu, A., 2010. Mid-Brunhes strengthening of
768 the Indian Ocean Dipole caused increased equatorial East African and decreased
769 Australasian rainfall. Geophys. Res. Lett. 37, L06706.
770 https://doi.org/10.1029/2009GL042225
771 Hastenrath, S., Nicklis, A., Greischar, L., 1993. Atmospheric-Hydrospheric mechanisms of
772 climate anomalies in the western equatorial Indian Ocean. J. Geophys. Res. 98, 20,219-

773 20,235. https://doi.org/10.1029/2004JD004981
774 Kim, S.-T., O'Neil, J.R., 1997. Equilibrium and nonequilibrium oxygen isotope effects in
775 synthetic carbonates. Geochim. Cosmochim. Acta 61, 3461–3475.
776 https://doi.org/10.1016/S0016-7037(97)00169-5
777 Krahmann, G., Krüger, K., 2018. Physical oceanography during SONNE cruise SO235.
778 PANGAEA. https://doi.org/10.1594/PANGAEA.887805
779 Kroon, D., Ganssen, G., 1989. Northern Indian Ocean upwelling cells and the stable isotope
780 composition of living planktonic foraminifers. Deep Sea Res. 36, 1219–1236.
781 https://doi.org/10.1016/0198-0149(89)90102-7
782 Kucera, M., 2007. Chapter Six planktonic foraminifera as tracers of past oceanic
783 environments, in: Developments in Marine Geology. pp. 213–262.
784 https://doi.org/10.1016/S1572-5480(07)01011-1
785 Kunkelova, T., Jung, S.J.A., de Leau, E.S., Odling, N., Thomas, A.L., Betzler, C., Eberli,
786 G.P., Alvarez-Zarikian, C.A., Alonso-García, M., Bialik, O.M., Blättler, C.L., Guo, J.A.,
787 Haffen, S., Horozal, S., Ling Hui Mee, A., Inoue, M., Jovane, L., Lanci, L., Laya, J.C.,
788 Lüdmann, T., Bejugam, N.N., Nakakuni, M., Niino, K., Petruny, L.M., Pratiwi, S.D.,
789 Reijmer, J.J.G., Reolid, J., Slagle, A.L., Sloss, C.R., Su, X., Swart, P.K., Wright, J.D.,
790 Yao, Z., Young, J.R., Lindhorst, S., Stainbank, S., Rueggeberg, A., Spezzaferri, S.,
791 Carrasqueira, I., Yu, S., Kroon, D., 2018. A two million year record of low-latitude
792 aridity linked to continental weathering from the Maldives. Prog. Earth Planet. Sci. 5, 86.
793 https://doi.org/10.1186/s40645-018-0238-x
794 Lisiecki, L.E., Raymo, M.E., 2005. A Pliocene-Pleistocene stack of 57 globally distributed
795 benthic $\delta^{18}O$ records. Paleoceanography 20, PA1003.
796 https://doi.org/10.1029/2004PA001071
797 Lüdmann, T., Kalvelage, C., Betzler, C., Fürstenau, J., Hübscher, C., 2013. The Maldives, a

giant isolated carbonate platform dominated by bottom currents. Mar. Pet. Geol. 43. https://doi.org/10.1016/j.marpetgeo.2013.01.004

O'Neil, J.R., Clayton, R.N., Mayeda, T.K., 1969. Oxygen isotope fractionation in divalent metal carbonates. J. Chem. Phys. 51, 5547–5558. https://doi.org/10.1063/1.1671982

Paillard, D., Labeyrie, L., Yiou, P., 1996. Macintosh program performs time-series analysis. Eos (Washington. DC). 77, 379. https://doi.org/10.1029/96eo00259

Panieri, G., Lepland, A., Whitehouse, M.J., Wirth, R., Raanes, M.P., James, R.H., Graves, C.A., Crémière, A., Schneider, A., 2017. Diagenetic Mg-calcite overgrowths on foraminiferal tests in the vicinity of methane seeps. Earth Planet. Sci. Lett. 458, 203–212. https://doi.org/10.1016/j.epsl.2016.10.024

Pearson, P.N., 2012. Oxygen isotopes in foraminifera: Overview and historical review, in: Ivany, L.C., Huber, B.T. (Eds.), Reconstructing Earth's Deep-Time Climate-The State of the Art in 2012, Paleontological Society Short Course, November 3. The Paleontological Society Papers, pp. 1–38.

Quadfasel, D., 2017. Physical oceanography during RV SONNE cruise SO127, 17 December 1997 to 7 January 1998 from Port Klang to Malé. PANGAEA. https://doi.org/10.1594/PANGAEA.881513

Raddatz, J., Nürnberg, D., Tiedemann, R., Rippert, N., 2017. Southeastern marginal West Pacific Warm Pool sea-surface and thermocline dynamics during the Pleistocene (2.5–0.5 Ma). Palaeogeogr. Palaeoclimatol. Palaeoecol. 471, 144–156. https://doi.org/10.1016/j.palaeo.2017.01.024

Rebotim, A., Voelker, A.H.L., Jonkers, L., Waniek, J.J., Meggers, H., Schiebel, R., Fraile, I., Schulz, M., Kucera, M., 2017. Factors controlling the depth habitat of planktonic foraminifera in the subtropical eastern North Atlantic. Biogeosciences 14, 827–859. https://doi.org/10.5194/bg-14-827-2017

823 Regenberg, M., Nürnberg, D., Schönfeld, J., Reichart, G.-J., 2007. Early diagenetic overprint
824 in Caribbean sediment cores and its effect on the geochemical composition of planktonic
825 foraminifera. Biogeosciences 4, 957–973. https://doi.org/10.5194/bg-4-957-2007
826 Reolid, J., Reolid, M., Betzler, C., Lindhorst, S., Wiesner, M.G., Lahajnar, N., 2017. Upper
827 Pleistocene cold-water corals from the Inner Sea of the Maldives: taphonomy and
828 environment. Facies 63, 8. https://doi.org/10.1007/s10347-016-0491-7
829 Rippert, N., Nürnberg, D., Raddatz, J., Maier, E., Hathorne, E., Bijma, J., Tiedemann, R.,
830 2016. Constraining foraminiferal calcification depths in the western Pacific warm pool.
831 Mar. Micropaleontol. 128, 14–27. https://doi.org/10.1016/j.marmicro.2016.08.004
832 Sadekov, A.Y., Ganeshram, R., Pichevin, L., Berdin, R., McClymont, E., Elderfield, H.,
833 Tudhope, A.W., 2013. Palaeoclimate reconstructions reveal a strong link between El
834 Niño-Southern Oscillation and Tropical Pacific mean state. Nat. Commun. 4, 2692.
835 https://doi.org/10.1038/ncomms3692
836 Schott, F.A., Xie, S.-P., McCreary Jr, J.P., 2009. Indian Ocean circulation and climate
837 variability. Rev. Geophys. 47, RG1002. https://doi.org/10.1029/2007RG000245
838 Sreevidya, E., Sijinkumar, A.V., Nath, B.N., 2019. Aragonite pteropod abundance and
839 preservation records from the Maldives, equatorial Indian Ocean: Inferences on past
840 oceanic carbonate saturation and dissolution events. Palaeogeogr. Palaeoclimatol.
841 Palaeoecol. 534, 109313. https://doi.org/10.1016/j.palaeo.2019.109313
842 Stainbank, S., Kroon, D., Rüggeberg, A., Raddatz, J., de Leau, E.S., Zhang, M., Spezzaferri,
843 S., 2019. Controls on planktonic foraminifera apparent calcification depths for the
844 northern equatorial Indian Ocean. PLoS One 14, e0222299.
845 https://doi.org/10.1371/journal.pone.0222299
846 Steinhardt, J., Cléroux, C., De Nooijer, L.J., Brummer, G.-J., Zahn, R., Ganssen, G., Reichart,
847 G.-J., 2015. Reconciling single-chamber Mg/Ca with whole-shell $\delta^{18}O$ in surface to

deep-dwelling planktonic foraminifera from the Mozambique Channel. Biogeosciences 12, 2411–2429. https://doi.org/10.5194/bg-12-2411-2015

Swart, P.K., 2015. The geochemistry of carbonate diagenesis: The past, present and future. Sedimentology 62, 1233–1304. https://doi.org/10.1111/sed.12205

Tarutani, T., Clayton, R.N., Mayeda, T.K., 1969. The effect of polymorphism and magnesium substitution on oxygen isotope fractionation between calcium carbonate and water. Geochim. Cosmochim. Acta 33, 987–996. https://doi.org/10.1016/0016-7037(69)90108-2

Wessel, P., Smith, W.H., 1991. Free software helps map and display data. Eos. Trans. AGU 72 (41), 441–446.

Supplementary Material 1. Representative visual SEM images used to define the Diagenesis Rank (DR) values for the individual species from IODP Expedition 359 Site U1467.

Supplementary Material 2. Electron Probe Micro-Analyzer (EPMA) data.

Supplementary Material 3. Secondary Ion Mass Spectrometer (SIMS) data.

Supplementary Material 4. Age model data for IODP Expedition 359 Site U1467.

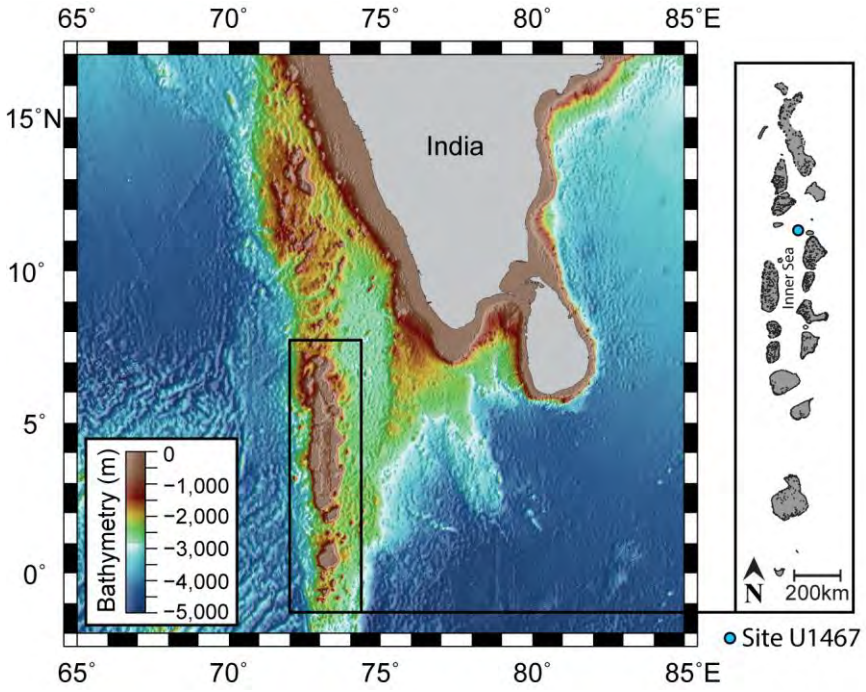
65°
70°
75°
80°
85°E
15°N
10°
5°
0°
India
Inner Sea
Bathymetry (m)
0
−1,000
−2,000
−3,000
−4,000
−5,000
N
200km
Site U1467

Fig. 1.

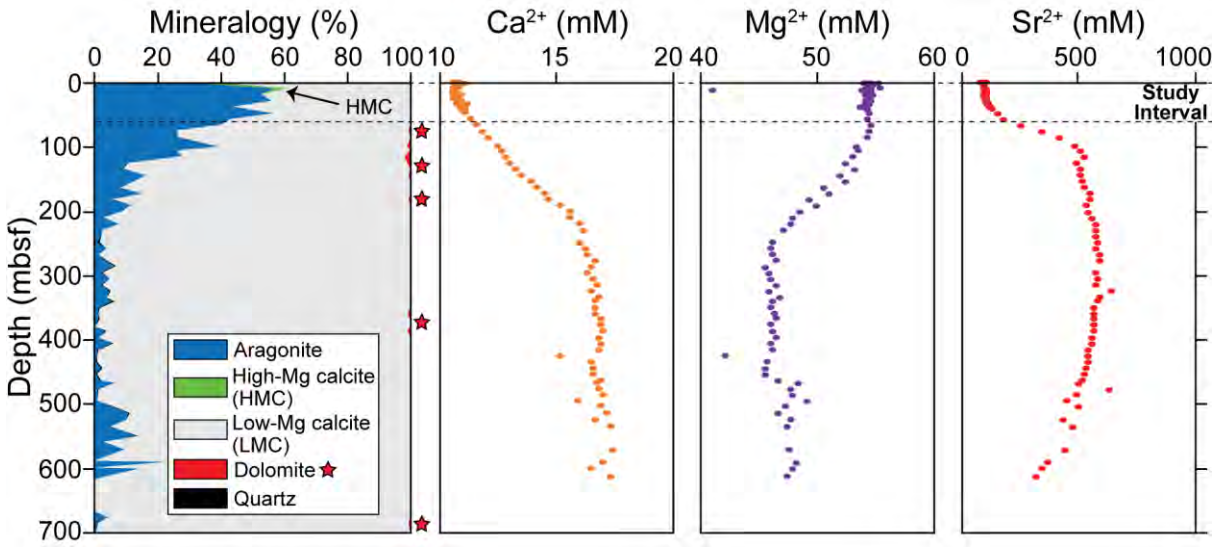
Mineralogy (%)
0
20
40
60
80
100
HMC
Depth (mbsf)
0
100
200
300
400
500
600
700
Aragonite
High-Mg calcite (HMC)
Low-Mg calcite (LMC)
Dolomite
Quartz
Ca2+ (mM)
10
15
20
Mg2+ (mM)
40
50
60
Sr2+ (mM)
0
500
1000
Study Interval

Fig. 2.

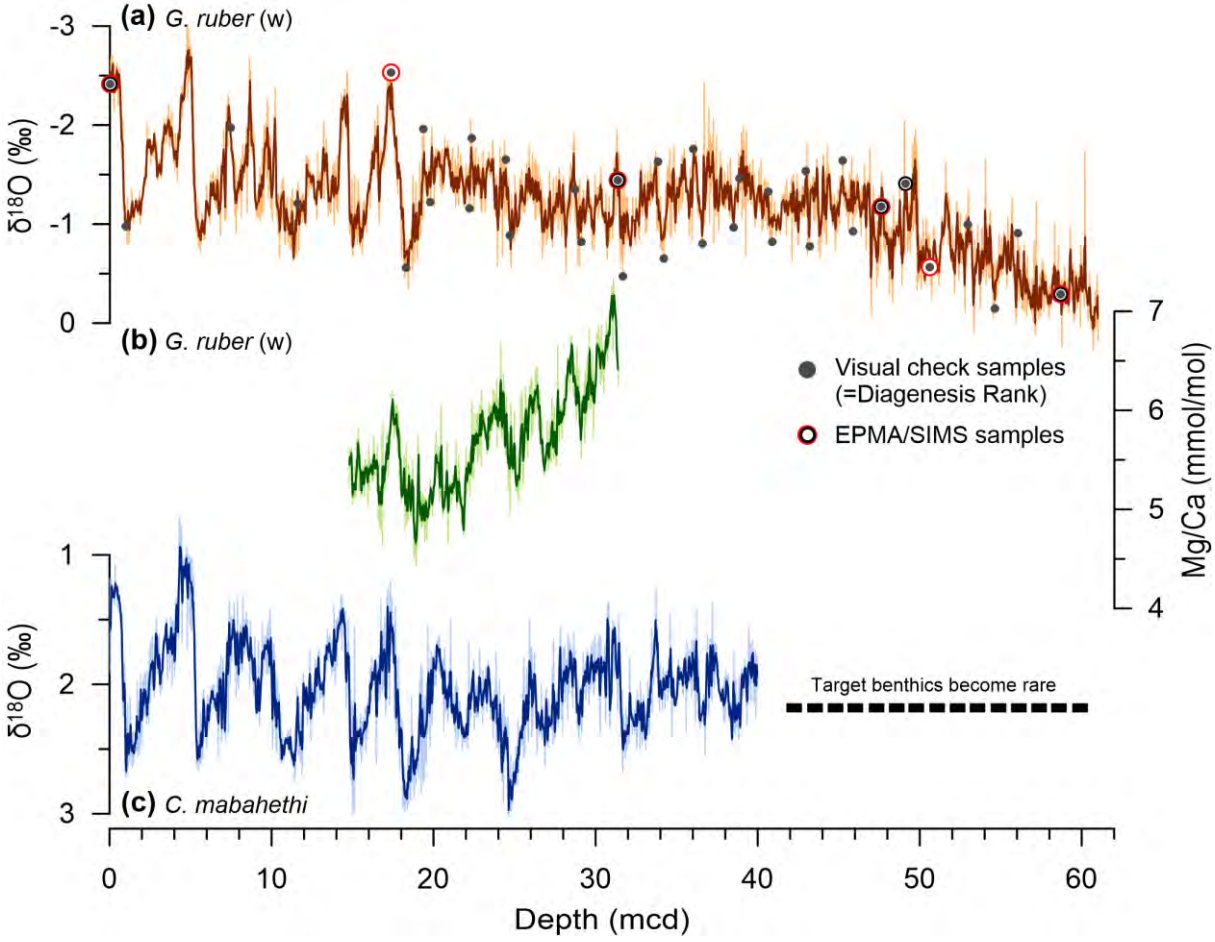
(a) G. ruber (w)
δ18O (‰)
-3
-2
-1
0
(b) G. ruber (w)
Visual check samples
(=Diagenesis Rank)
EPMA/SIMS samples
Mg/Ca (mmol/mol)
7
6
5
4
1
2
3
δ18O (‰)
(c) C. mabahethi
Target benthics become rare
0
10
20
30
40
50
60
Depth (mcd)

Fig. 3.

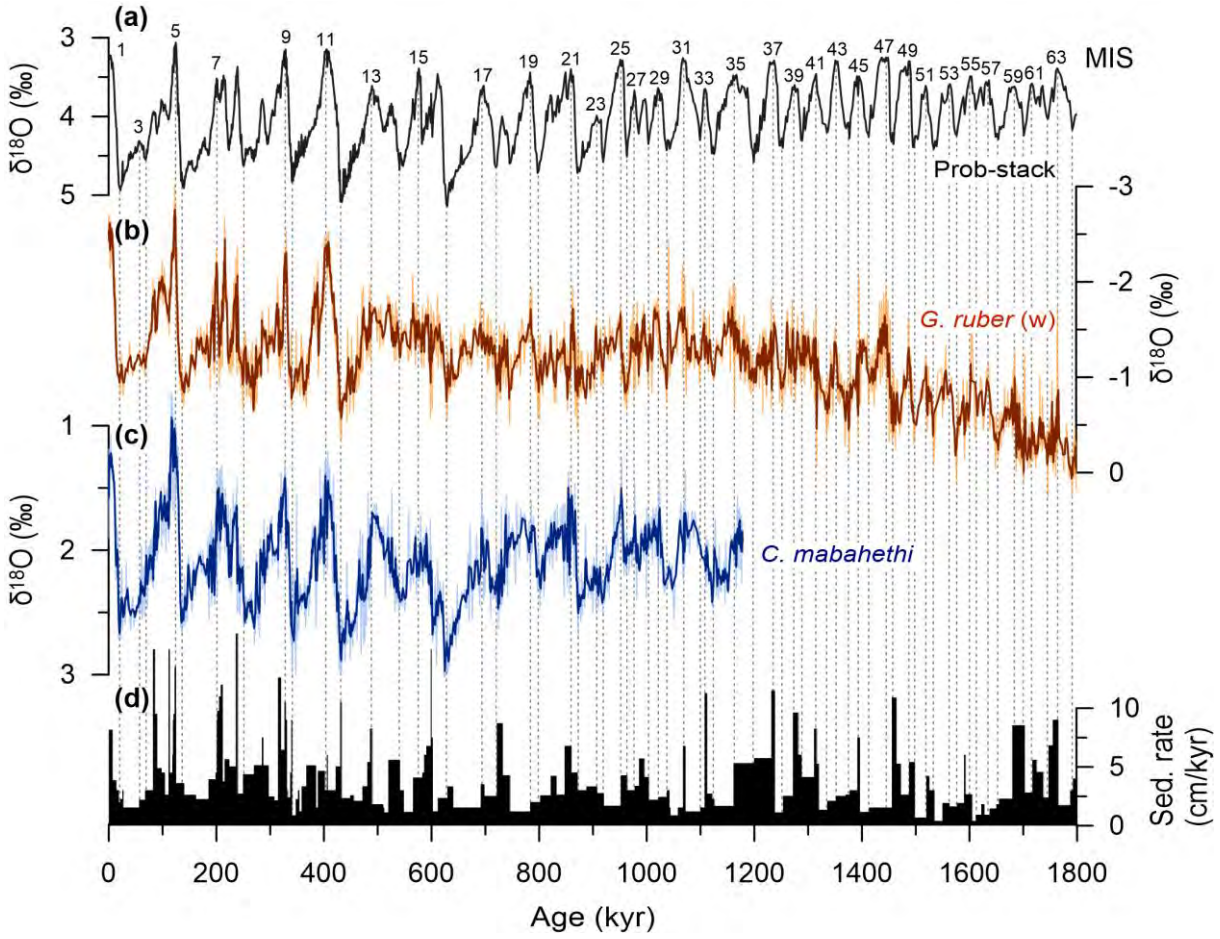
(a)
(b)
(c)
(d)
MIS
Prob-stack
G. ruber (w)
C. mabahethi
δ18O (‰)
Sed. rate (cm/kyr)
Age (kyr)
0
200
400
600
800
1000
1200
1400
1600
1800

Fig. 4.

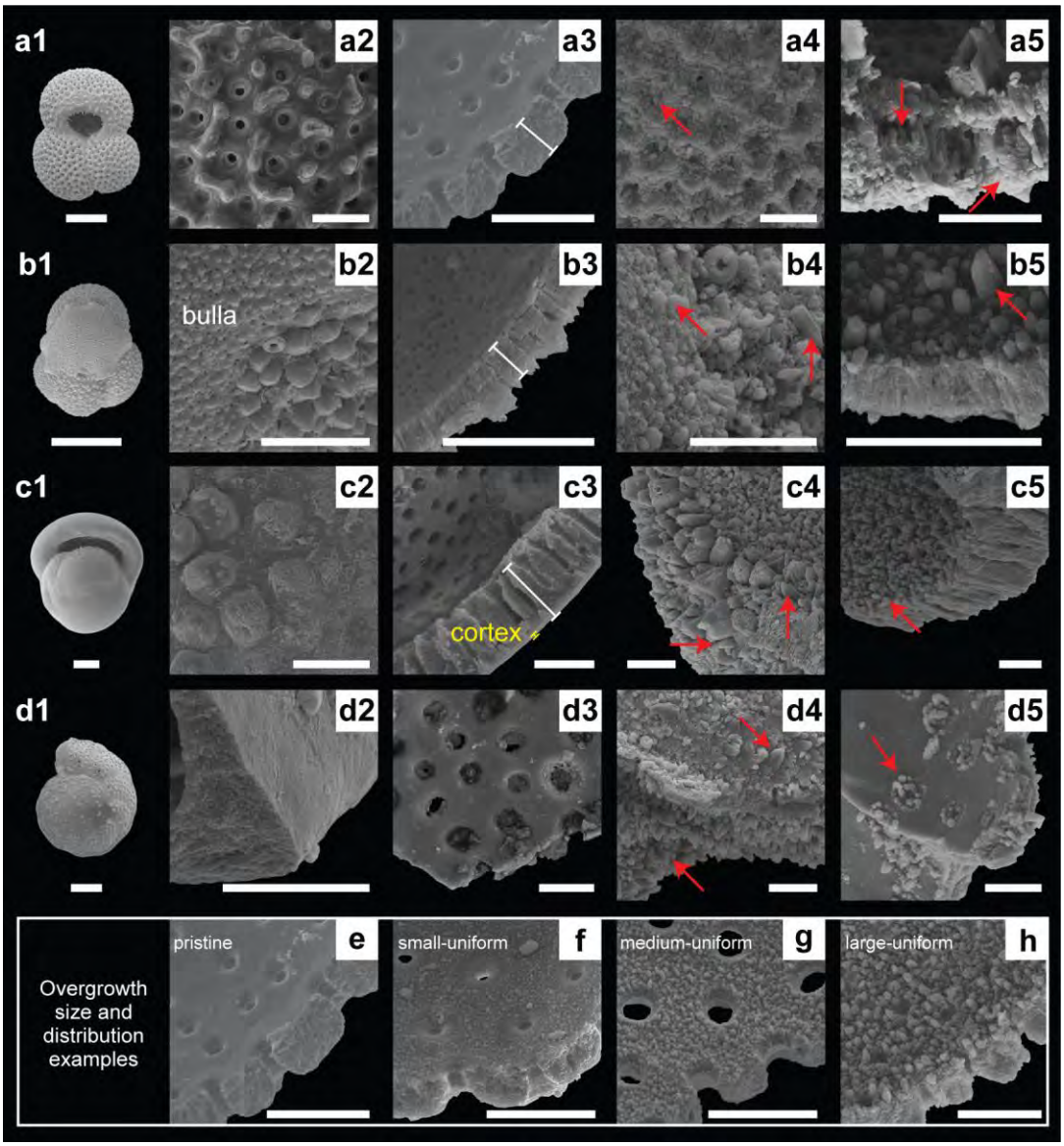
a1
a2
a3
a4
a5
b1
b2
bulla
b3
b4
b5
c1
c2
c3
cortex
c4
c5
d1
d2
d3
d4
d5
Overgrowth size and distribution examples
pristine
e
small-uniform
f
medium-uniform
g
large-uniform
h

Fig. 5.

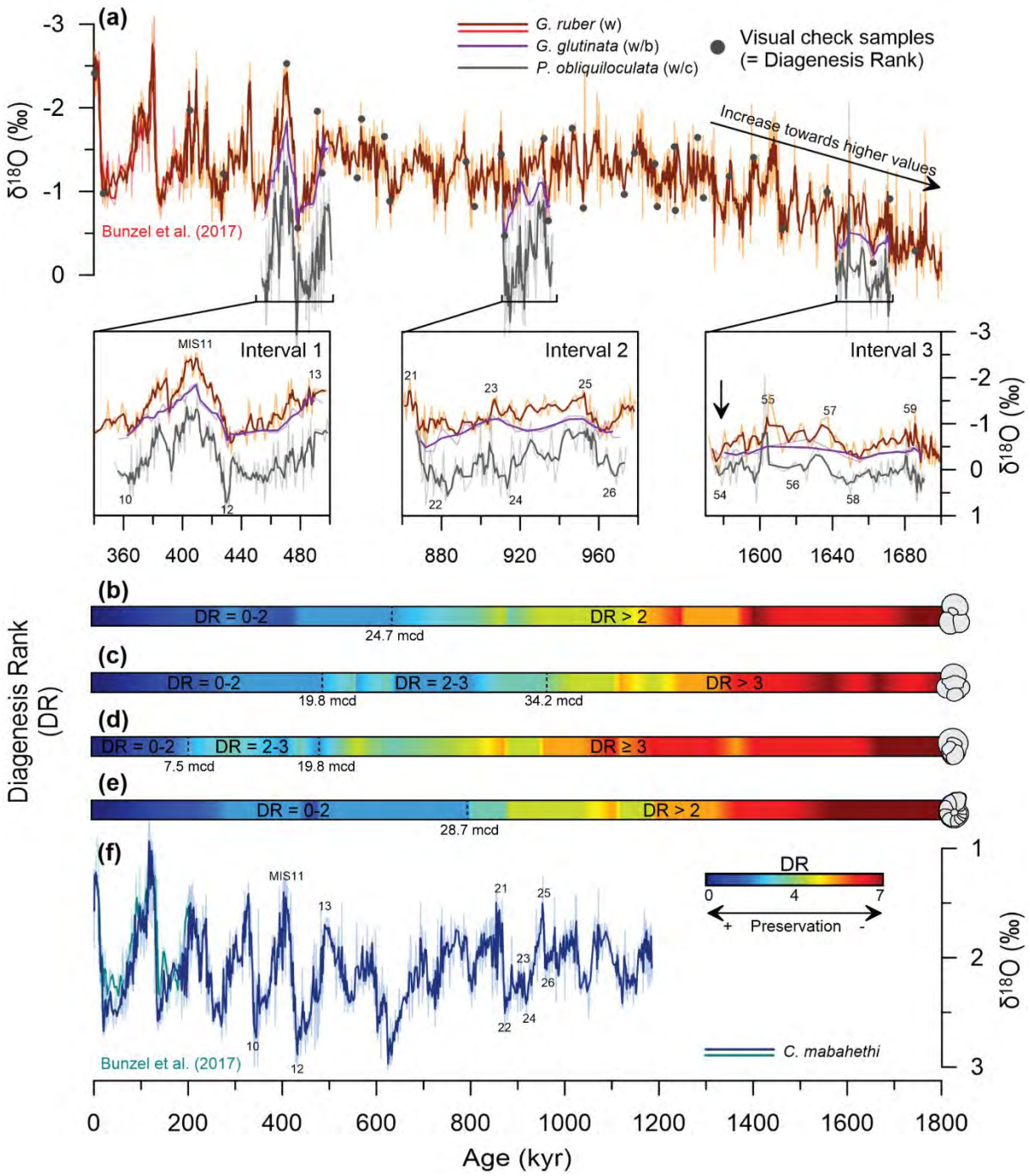
(a)
G. ruber (w)
G. glutinata (w/b)
P. obliquiloculata (w/c)
Visual check samples
(= Diagenesis Rank)
Increase towards higher values
Bunzel et al. (2017)
δ18O (‰)
Interval 1
Interval 2
Interval 3
MIS11
(b)
DR = 0-2
DR > 2
24.7 mcd
(c)
DR = 0-2
DR = 2-3
DR > 3
19.8 mcd
34.2 mcd
(d)
DR = 0-2
DR = 2-3
DR ≥ 3
7.5 mcd
19.8 mcd
(e)
DR = 0-2
DR > 2
28.7 mcd
Diagenesis Rank (DR)
(f)
DR
Preservation
C. mabahethi
Bunzel et al. (2017)
Age (kyr)

Fig. 6.

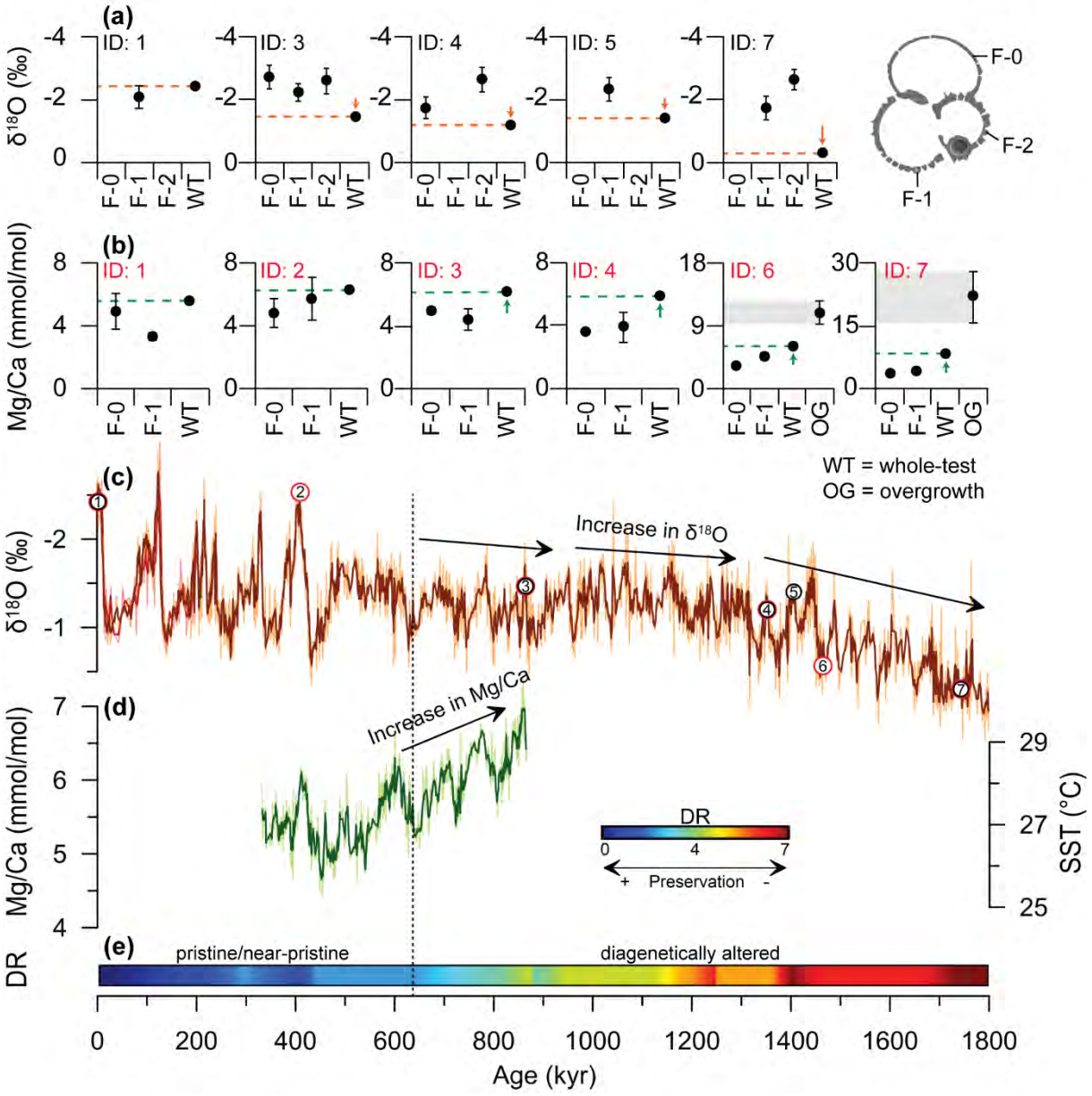
(a)
δ18O (‰)
ID: 1
ID: 3
ID: 4
ID: 5
ID: 7
F-0
F-1
F-2
WT
(b)
Mg/Ca (mmol/mol)
ID: 1
ID: 2
ID: 3
ID: 4
ID: 6
ID: 7
OG
WT = whole-test
OG = overgrowth
(c)
δ18O (‰)
Increase in δ18O
(d)
Mg/Ca (mmol/mol)
Increase in Mg/Ca
DR
Preservation
SST (°C)
(e)
pristine/near-pristine
diagenetically altered
Age (kyr)

Fig. 7.

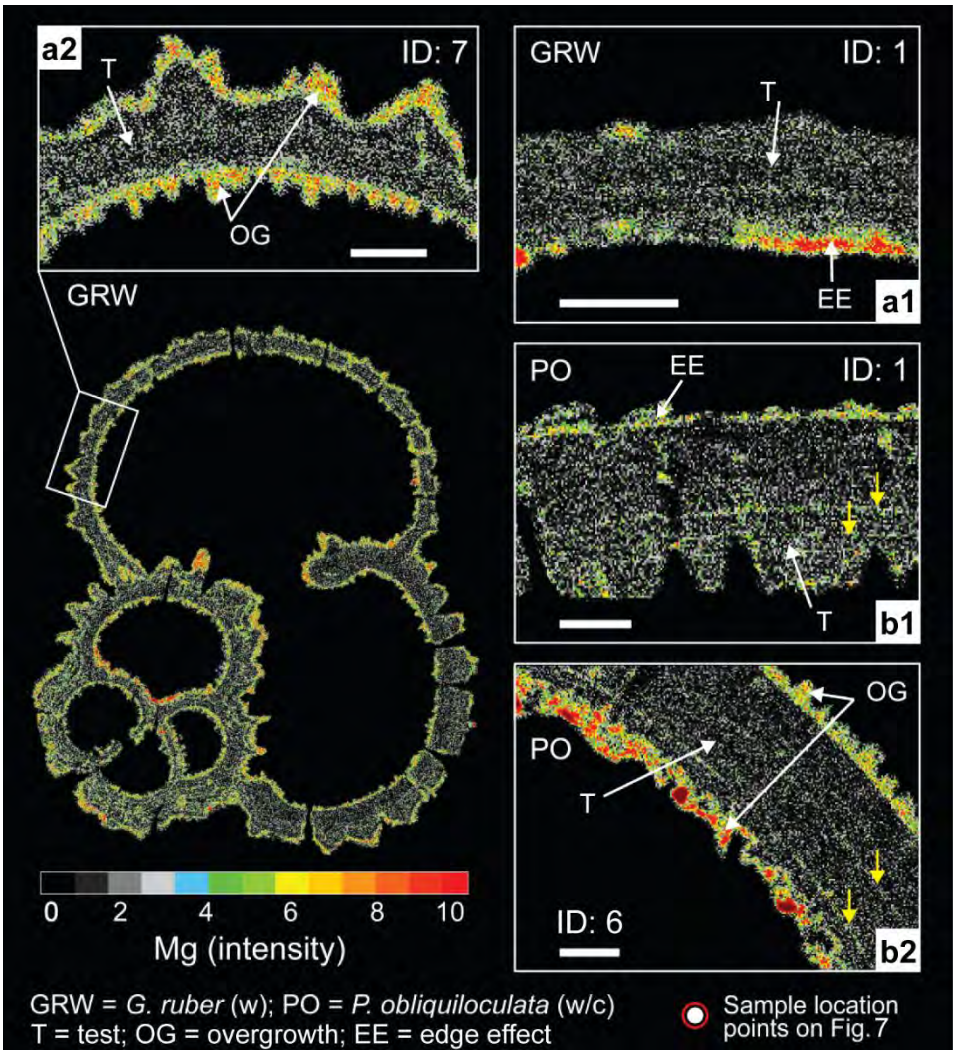
a2
T
ID: 7
OG
GRW
GRW
ID: 1
T
EE
a1
PO
EE
ID: 1
T
b1
OG
PO
T
ID: 6
b2
0 2 4 6 8 10
Mg (intensity)
GRW = G. ruber (w); PO = P. obliquiloculata (w/c)
T = test; OG = overgrowth; EE = edge effect
Sample location points on Fig. 7

Fig. 8.

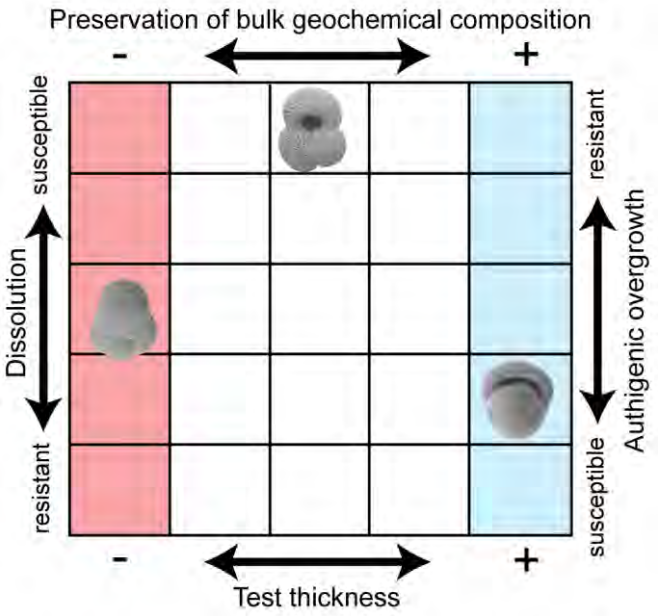
Preservation of bulk geochemical composition
-
+
susceptible
resistant
Dissolution
Authigenic overgrowth
resistant
susceptible
-
+
Test thickness

Fig. 9.

Supplementary Material 1. Representative visual SEM images used to define the Diagenesis Rank (DR) values for the individual species from IODP Expedition 359 Site U1467.

Supplementary Figs. 1a–b.

IODP Expedition 359 Site U1467 cross section and inner test surface SEM images of (a) *G. ruber* (w); (b) *G. glutinata* (w/b); (c) *P. obliquiloculata* (w/c) and (d) *C. mabahethi/wuellerstorfi* for Samples: (1) A, B-Mudline; (2) C-1H-1, 99-100 cm; (3) B-3H-3, 9-10 cm; (4) B-3H-3, 102-103 cm; (5) B-4H-5, 36-37 cm; (6) C-4H-3, 87-88 cm; (7) C-5H-4, 30-31 cm; (8) B-6H-2, 75-76 cm; (9) B-6H-3, 75-76 cm; (10) B-6H-4, 75-76 cm; (11) C-6H-5, 57-58 cm; (12) B-7H-3, 75-76 cm. For reference, SIMS and EPMA Samples 1-7 are indicated in the black and red circles, respectively. White bars indicate test thickness. Scale bars = 20 μm.

Supplementary Figs. 1c–d.

IODP Expedition 359 Site U1467 external test surface SEM images of (e) *G. ruber* (w); (f) *G. glutinata* (w/b); (g) *P. obliquiloculata* (w/c) and (h) *C. mabahethi/wuellerstorfi* for Samples: (1) A, B-Mudline; (2) C-1H-1, 99-100 cm; (3) B-3H-3, 9-10 cm; (4) B-3H-3, 102-103 cm; (5) B-4H-5, 36-37 cm; (6) C-4H-3, 87-88 cm; (7) C-5H-4, 30-31 cm; (8) B-6H-2, 75-76 cm; (9) B-6H-3, 75-76 cm; (10) B-6H-4, 75-76 cm; (11) C-6H-5, 57-58 cm; (12) B-7H-3, 75-76 cm. For reference, SIMS and EPMA Samples 1-7 are indicated in the black and red circles, respectively. Scale bars = 20 μm.

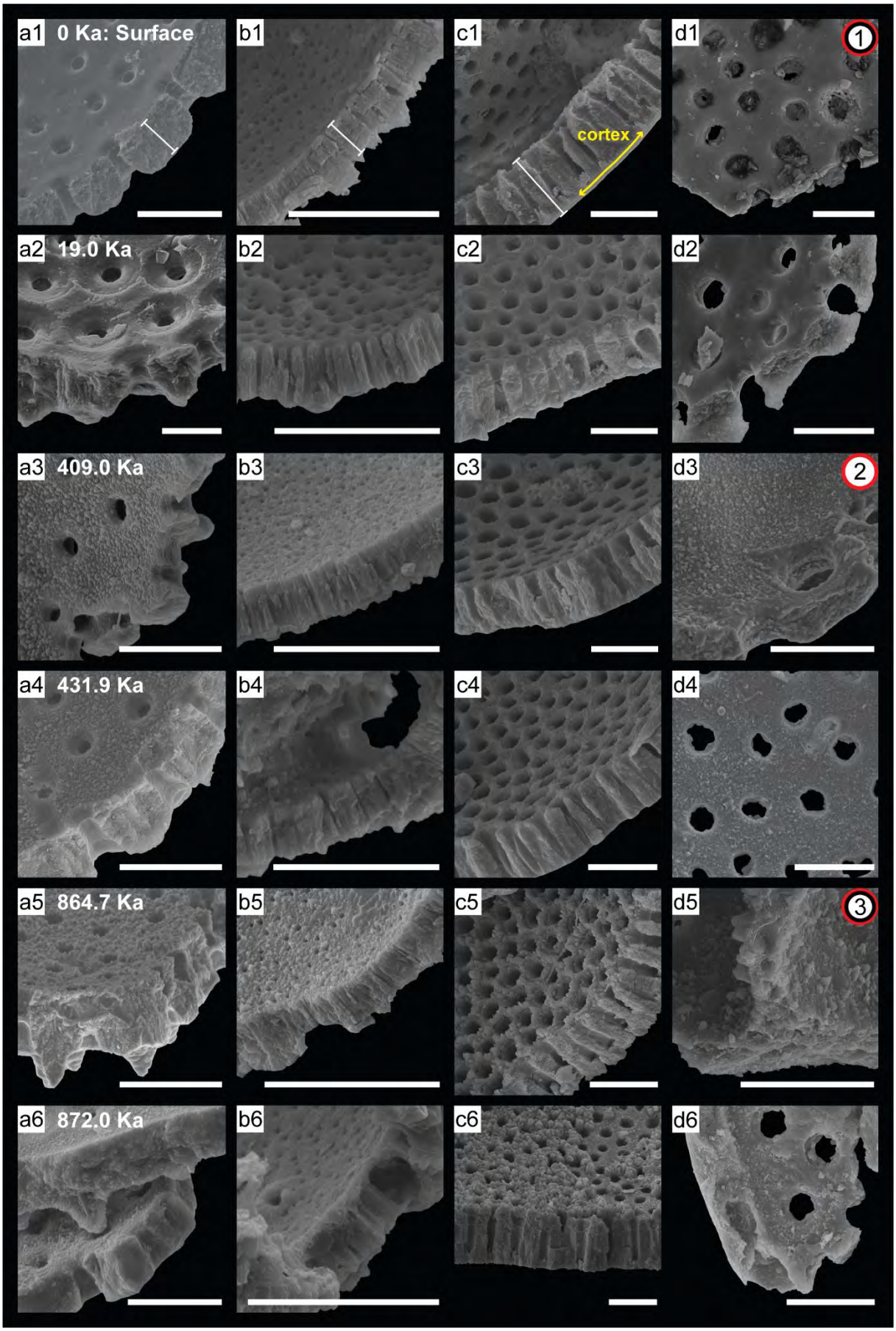

Supplementary Fig. 1a.

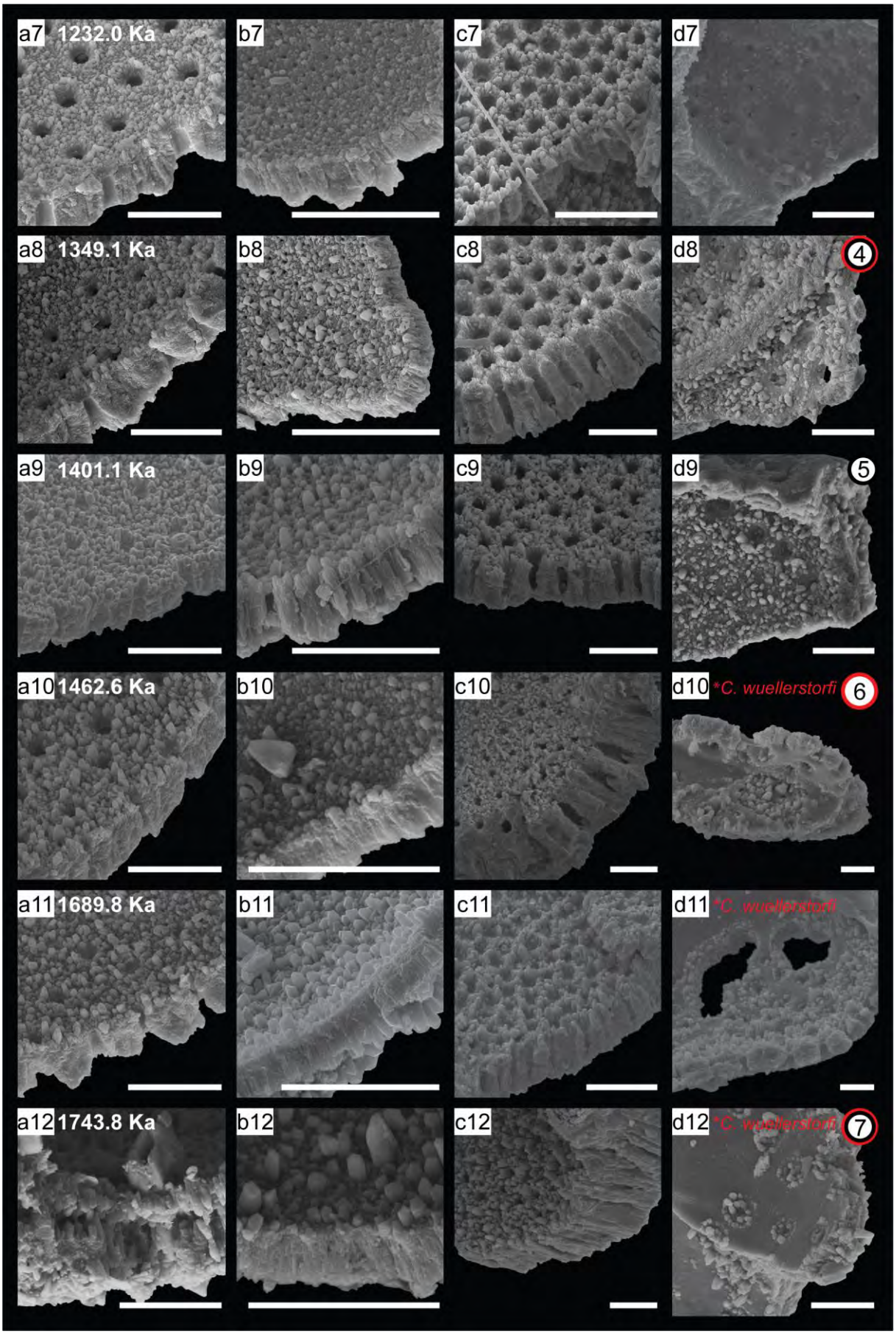

Supplementary Fig. 1b.

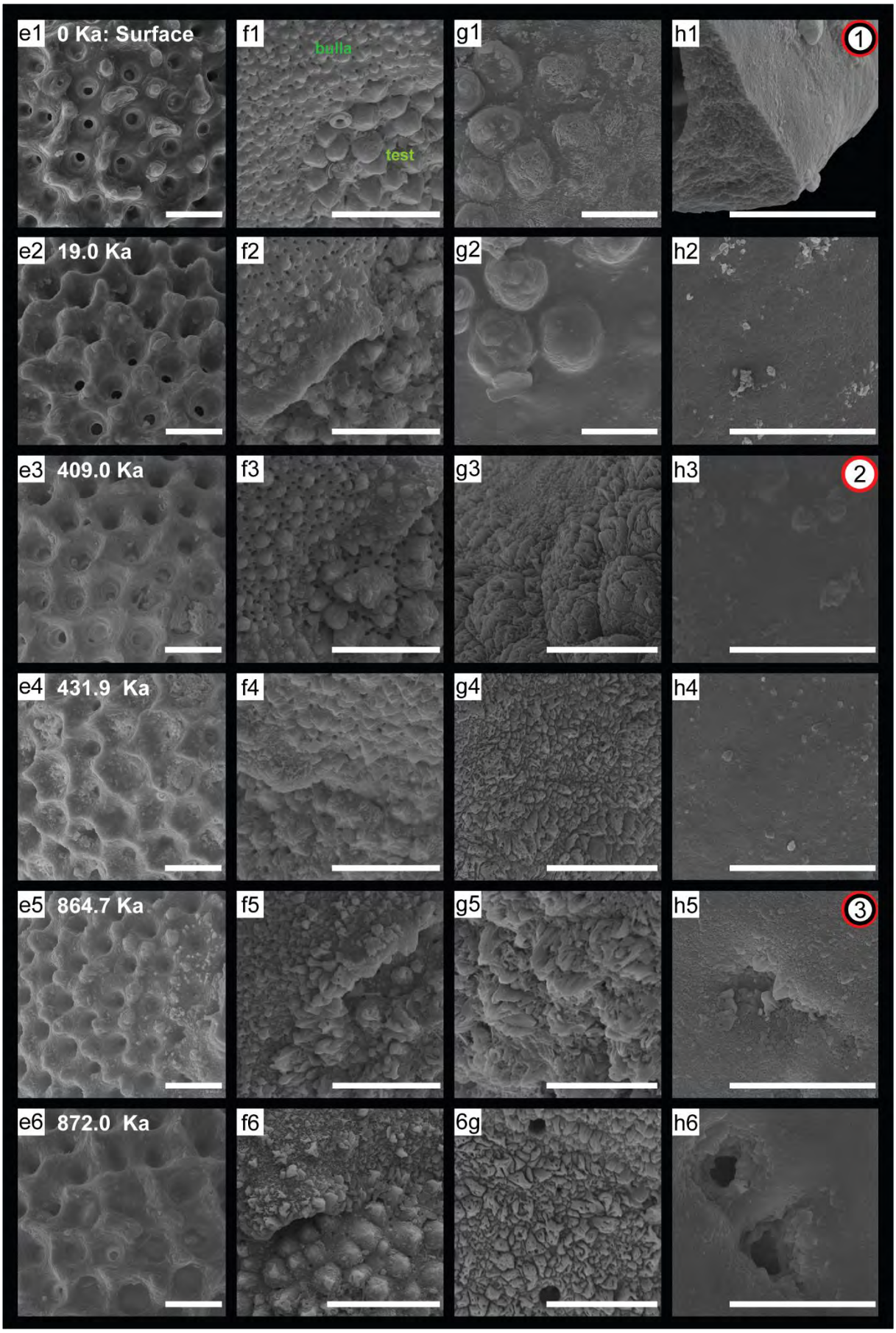

Supplementary Fig. 1c.

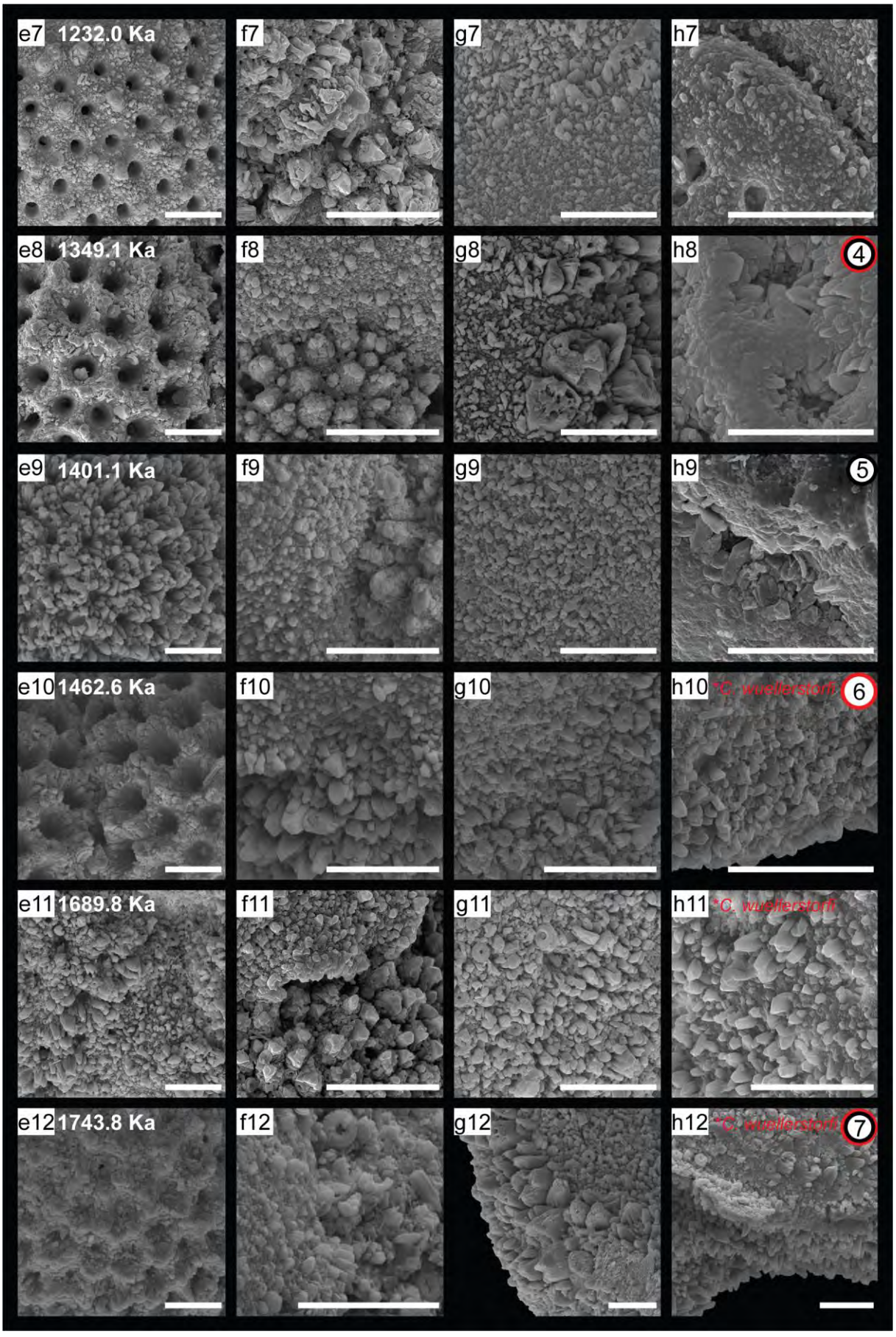

Supplementary Fig. 1d.

Supplementary Material 2. Electron Probe Micro-Analyzer (EPMA) data.

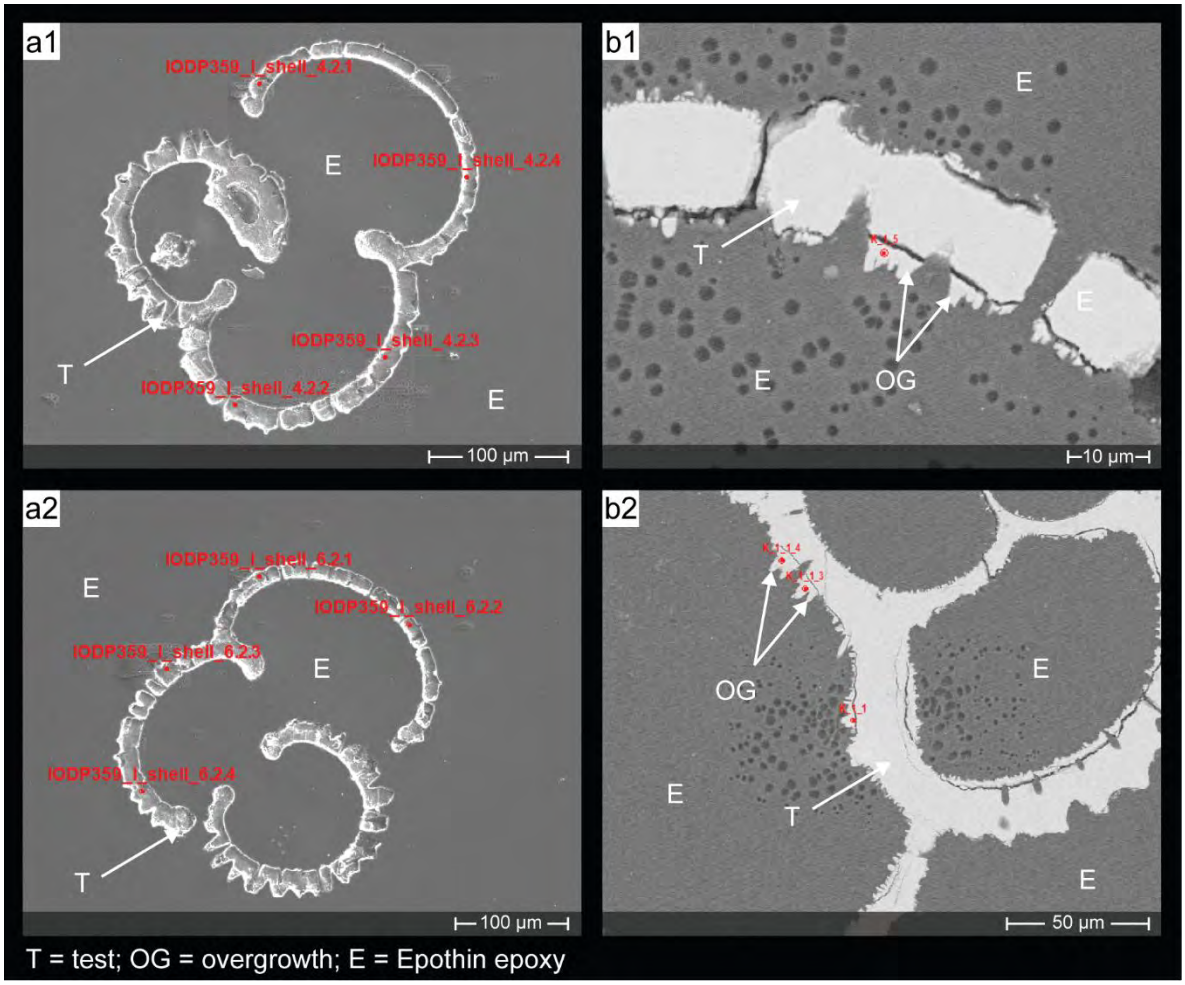

Supplementary Fig. 2a. IODP Expedition 359 Site U1467 *G. ruber* (w) SEM images showing examples of EPMA spot measurements for (a) the foraminifera test (T) and (b) large authigenic overgrowths (OG). Samples: (a1) B-4H-5, 36-37 cm; a2) B-6H-2, 75-76 cm; (b1-2) B-6H-4, 75-76 cm (Approximate location of the EPMA spots are shown for reference with the red dots with the red text indicating their individual EPMA IDs).

Supplementary Table 2a. IODP Expedition 359 Site U1467 *G. ruber* (w) EPMA test measurements used in the study. Measurements with total counts < 97 and > 102 were excluded. Note: SrO was measured for all samples and was zero in all instances.

Sample	EPMA ID	Sample ID	CaO	MgO	C	Total	Chamber	Mg/Ca (mmol/mol)
359-U1467B-Mudline	IODP359_I_shell_1.1.1	1	56.45	0.21	44.53	101.19	F-0	5.17
359-U1467B-Mudline	IODP359_I_shell_1.1.2		56.00	0.26	44.24	100.50	F-0	6.49
359-U1467B-Mudline	IODP359_I_shell_1.2.3		55.23	0.19	43.55	98.97	F-0	4.87
359-U1467B-Mudline	IODP359_I_shell_1.2.4		55.17	0.13	43.44	98.74	F-0	3.25
359-U1467B-Mudline	IODP359_I_shell_1.1.3		55.86	0.13	43.98	99.97	F-1	3.17
359-U1467B-Mudline	IODP359_I_shell_1.1.4		55.40	0.12	43.61	99.13	F-1	3.11
359-U1467B-Mudline	IODP359_I_shell_1.2.2		55.74	0.15	43.91	99.80	F-1	3.70
359-U1467B-3H-3, 9-10 cm	IODP359_I_shell_2.1.1	2	55.55	0.18	43.79	99.52	F-0	4.51
359-U1467B-3H-3, 9-10 cm	IODP359_I_shell_2.1.2		56.30	0.26	44.47	101.03	F-0	6.43
359-U1467B-3H-3, 9-10 cm	IODP359_I_shell_2.2.1		55.37	0.18	43.65	99.20	F-0	4.45
359-U1467B-3H-3, 9-10 cm	IODP359_I_shell_2.2.2		55.41	0.16	43.66	99.23	F-0	3.90
359-U1467B-3H-3, 9-10 cm	IODP359_I_shell_2.1.3		54.98	0.29	43.46	98.73	F-1	7.36
359-U1467B-3H-3, 9-10 cm	IODP359_I_shell_2.1.4		54.82	0.24	43.28	98.34	F-1	6.14
359-U1467B-3H-3, 9-10 cm	IODP359_I_shell_2.2.3		55.31	0.14	43.56	99.01	F-1	3.54
359-U1467B-3H-3, 9-10 cm	IODP359_I_shell_2.2.4		54.71	0.23	43.18	98.12	F-1	5.83
359-U1467B-4H-5, 36-37 cm	IODP359_I_shell_4.1.2	3	54.96	0.21	43.36	98.53	F-0	5.20
359-U1467B-4H-5, 36-37 cm	IODP359_I_shell_4.2.4		55.13	0.19	43.47	98.79	F-0	4.81
359-U1467B-4H-5, 36-37 cm	IODP359_I_shell_4.1.3		55.01	0.20	43.39	98.60	F-1	5.15
359-U1467B-4H-5, 36-37 cm	IODP359_I_shell_4.2.2		55.60	0.14	43.79	99.53	F-1	3.51
359-U1467B-4H-5, 36-37 cm	IODP359_I_shell_4.2.3		55.75	0.18	43.95	99.88	F-1	4.48
359-U1467B-6H-2, 75-76 cm	IODP359_I_shell_6.1.1	4	55.08	0.14	43.39	98.61	F-0	3.64
359-U1467B-6H-2, 75-76 cm	IODP359_I_shell_6.1.3		55.17	0.13	43.44	98.74	F-1	3.32
359-U1467B-6H-2, 75-76 cm	IODP359_I_shell_6.1.4		55.90	0.12	44.00	100.02	F-1	2.96
359-U1467B-6H-2, 75-76 cm	IODP359_I_shell_6.1.5		55.75	0.15	43.92	99.82	F-1	3.79
359-U1467B-6H-2, 75-76 cm	IODP359_I_shell_6.2.4		55.10	0.21	43.47	98.78	F-1	5.41
359-U1467B-6H-4, 75-76 cm	IODP359_I_shell_8.1.2	6	56.90	0.13	44.79	101.82	F-0	3.11
359-U1467B-6H-4, 75-76 cm	IODP359_I_shell_8.3.1		55.22	0.15	43.50	98.87	F-0	3.74
359-U1467B-6H-4, 75-76 cm	IODP359_I_shell_8.1.4		55.32	0.16	43.59	99.07	F-1	4.08
359-U1467B-6H-4, 75-76 cm	IODP359_I_shell_8.3.3		55.49	0.19	43.76	99.44	F-1	4.77
359-U1467B-6H-4, 75-76 cm	IODP359_I_shell_8.3.4		54.92	0.22	43.34	98.48	F-1	5.53
359-U1467B-7H-3, 75-76 cm	IODP359_I_shell_9.1.1	7	56.78	0.14	44.72	101.64	F-0	3.49
359-U1467B-7H-3, 75-76 cm	IODP359_I_shell_9.1.2		55.74	0.15	43.90	99.79	F-0	3.66
359-U1467B-7H-3, 75-76 cm	IODP359_I_shell_9.1.6		55.13	0.12	43.40	98.65	F-1	3.13
359-U1467B-7H-3, 75-76 cm	IODP359_I_shell_9.2.3		55.09	0.18	43.43	98.70	F-1	4.43
359-U1467B-7H-3, 75-76 cm	IODP359_I_shell_9.2.4		55.42	0.17	43.68	99.27	F-1	4.18
359-U1467B-7H-3, 75-76 cm	IODP359_I_shell_9.2.5		54.66	0.17	43.08	97.91	F-1	4.33

Supplementary Table 2b. IODP Expedition 359 Site U1467 *G. ruber* (w) EPMA overgrowth measurements used in the study. Measurements with total counts < 97 and > 102 were excluded. Note: SrO was measured for all samples and was zero in all instances.

Sample	EPMA ID	Sample ID	CaO	MgO	C	Total	Mg/Ca (mmol/mol)
359-U1467B-6H-4, 75-76 cm	K_1_1	6	54.70	0.55	43.52	98.77	13.87
359-U1467B-6H-4, 75-76 cm	K_1_1_4		56.29	0.41	44.62	101.32	10.13
359-U1467B-7H-3, 75-76 cm	K_5_2	7	56.19	0.53	44.67	101.39	13.12
359-U1467B-7H-3, 75-76 cm	K_5_2_b		54.80	1.05	44.15	100.00	26.71
359-U1467B-7H-3, 75-76 cm	K_5_1		54.76	1.01	44.08	99.85	25.76

Supplementary Table 2c. IODP Expedition 359 Site U1467 whole-test *G. ruber* (w) Mg/Ca data used in EPMA comparison.*Data is taken from Stainbank et al. (2019).

Sample	Sample ID	Mg/Ca (mmol/mol)
359-U1467B-Mudline	1	5.66*
359-U1467B-Mudline		5.65*
359-U1467B-3H-3, 9-10 cm	2	6.30
359-U1467B-3H-3, 9-10 cm		6.00
359-U1467B-3H-3, 9-10 cm		5.97
359-U1467B-4H-5, 36-37 cm	3	6.18
359-U1467B-4H-5, 36-37 cm		6.22
359-U1467B-6H-2, 75-76 cm	4	6.05
359-U1467B-6H-2, 75-76 cm		5.72
359-U1467B-6H-4, 75-76 cm	6	6.62
359-U1467B-6H-4, 75-76 cm		6.10
359-U1467B-7H-3, 75-76 cm	7	8.45
359-U1467B-7H-3, 75-76 cm		7.32

Supplementary Material 3. Secondary Ion Mass Spectrometer (SIMS) data.

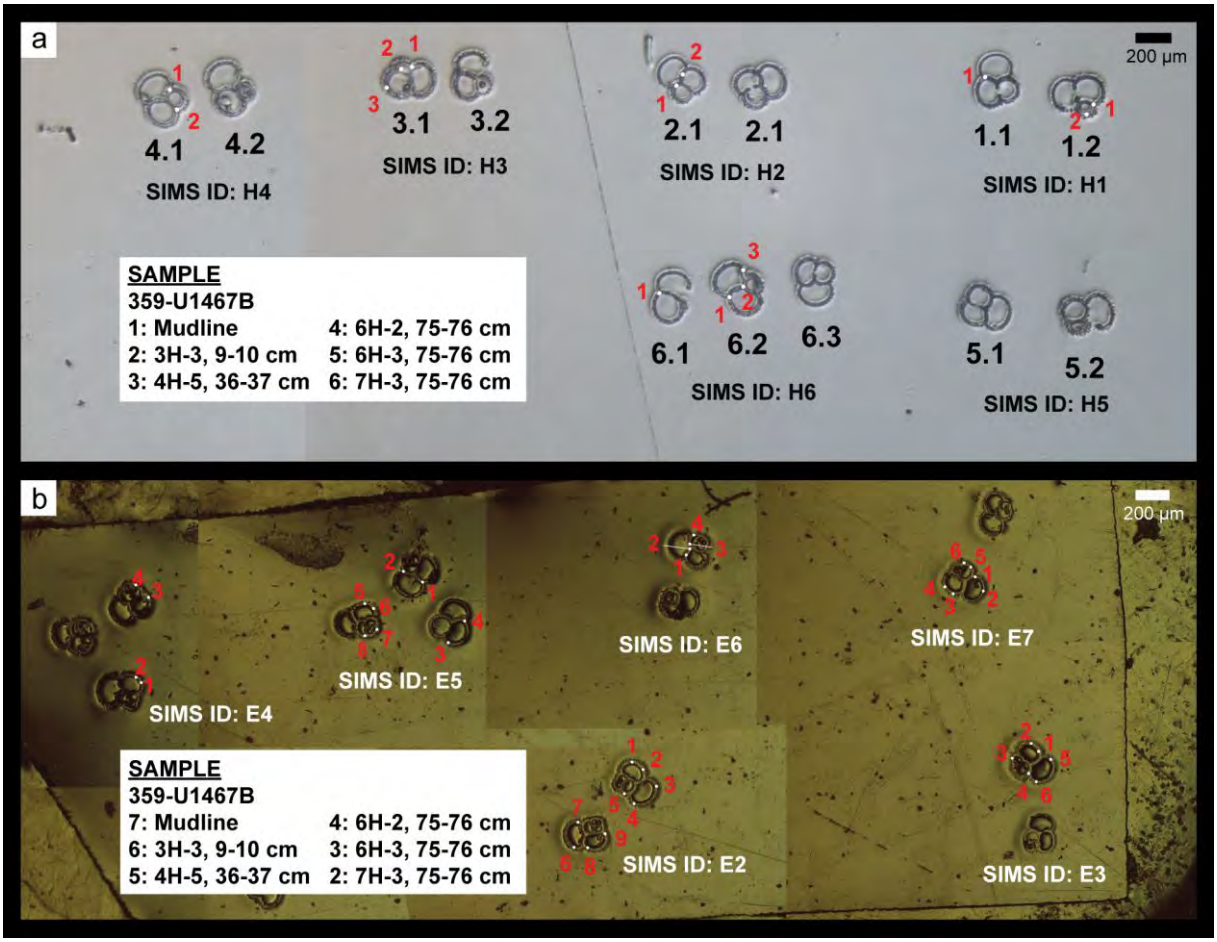

Supplementary Fig. 3a. Compilation of IODP Expedition 359 Site U1467 (a) stereomicroscope images of embedded and polished *G. ruber* (w) SIMS Sample H showing approximate SIMS spot locations and (b) transmitted light microscope images of *G. ruber* (w) SIMS Sample E showing approximate SIMS spot locations. Sample IDs are indicated on the image.

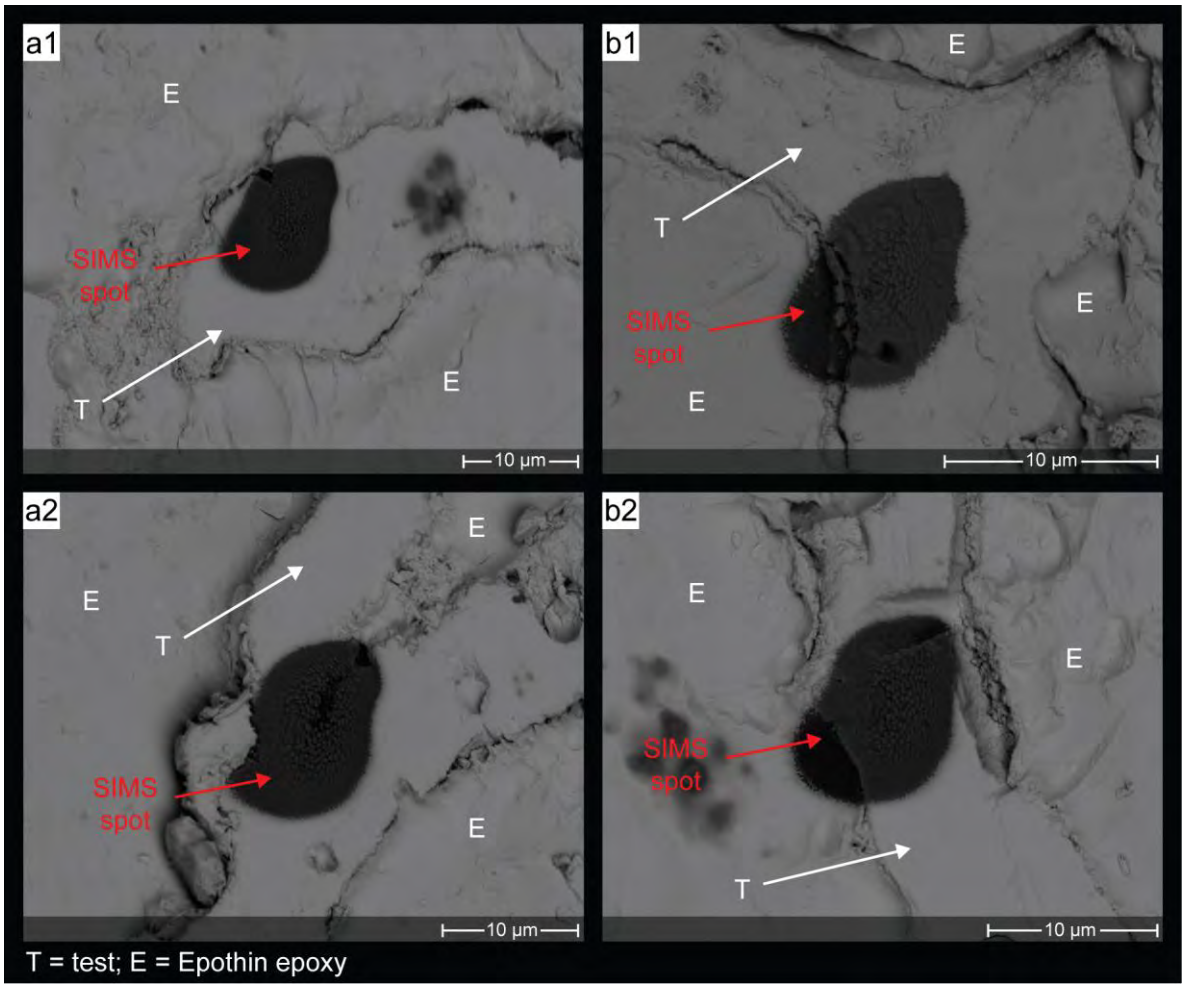

Supplementary Fig. 3b. IODP Expedition 359 Site U1467 SEM images showing examples of *G. ruber* (w) SIMS spots which (a) hit only the foraminiferal test (T) and (b) which partly hit the epoxy (E). IODP Expedition 359 Site U1467 Samples: (a1) B-4H-5, 36-37 cm (SIMS ID: δ^{18}O_foram_H3_1@1); (a2) B-6H-2, 75-76 cm (SIMS ID: δ^{18}O_foram_H4_1@1); (b1) B-Mudline (SIMS ID: δ^{18}O_foram_H1_2@1); (b2) B-4H-5, 36-37 cm (SIMS ID: δ^{18}O_foram_H3_1@3).

Supplementary Table 3a. IODP Expedition 359 Site U1467 *G. ruber* (w) SIMS measurement spots, which hit no epoxy and were used in the study. (Session H-1 standard yield: 1.10E+09; Session E-2 standard yield: 9.30E+08). Bold indicates the SIMS spot, which hit substantial authigenic overgrowth.

Sample	SIMS ID	Sample ID	Session	Yield	$\delta^{18}O$ (‰)	2se (‰)	Chamber
359-U1467B-Mudline	$\delta^{18}O$_foram_E7@4	1	E-2	1.021E+09	-2.08	0.35	F-1
359-U1467B-4H-5, 36-37 cm	$\delta^{18}O$_foram_H3_1@1	3	H-1	1.093E+09	-2.70	0.38	F-0
359-U1467B-4H-5, 36-37 cm	$\delta^{18}O$_foram_E5@6		E-2	8.728E+08	-2.22	0.29	F-1
359-U1467B-4H-5, 36-37 cm	$\delta^{18}O$_foram_E5@7		E-2	9.644E+08	-2.14	0.39	F-2
359-U1467B-4H-5, 36-37 cm	$\delta^{18}O$_foram_E5@8		E-2	9.468E+08	-2.81	0.30	F-2
359-U1467B-4H-5, 36-37 cm	$\delta^{18}O$_foram_H3_1@2		H-1	1.043E+09	-2.82	0.50	F-2
359-U1467B-6H-2, 75-76 cm	$\delta^{18}O$_foram_H4_1@1	4	H-1	1.049E+09	-1.75	0.35	F-0/F-2
359-U1467B-6H-2, 75-76 cm	$\delta^{18}O$_foram_H4_1@2		H-1	1.065E+09	-2.63	0.38	F-2
359-U1467B-6H-3, 75-76 cm	$\delta^{18}O$_foram_E3@1	5	E-2	1.078E+09	-2.15	0.34	F-1
359-U1467B-6H-3, 75-76 cm	$\delta^{18}O$_foram_E3@2		E-2	9.996E+08	-2.51	0.43	F-1
359-U1467B-7H-3, 75-76 cm	$\delta^{18}O$_foram_E2@1	7	E-2	9.859E+08	-1.55	0.44	F-1
359-U1467B-7H-3, 75-76 cm	$\delta^{18}O$_foram_E2@2		E-2	9.881E+08	-2.18	0.39	F-1
359-U1467B-7H-3, 75-76 cm	$\delta^{18}O$_foram_H6_1@1		H-1	1.045E+09	-2.00	0.26	F-1
359-U1467B-7H-3, 75-76 cm	**$\delta^{18}O$_foram_H6_2@1**		**H-1**	**9.555E+08**	**-1.24**	**0.41**	**F-1**
359-U1467B-7H-3, 75-76 cm	$\delta^{18}O$_foram_H6_2@2		H-1	1.025E+09	-3.15	0.38	F-2
359-U1467B-7H-3, 75-76 cm	$\delta^{18}O$_foram_H6_2@3		H-1	1.035E+09	-2.12	0.27	F-2

Supplementary Material 4. Table 4a. Age model data for IODP Expedition 359 Site U1467

Tie-points

359-U1467B, C Depth (mcd)	Prob-stack (Ahn et al., 2017) Age (kyr)	Sedimentation rate (cm/kyr)
0.01	0	8.1
0.58	7	3.9
0.85	14	3.0
1.00	19	2.0
1.06	22	2.3
1.15	26	3.0
1.18	27	1.5
1.63	57	2.2
1.87	68	3.0
2.32	83	15.0
2.77	86	9.5
3.15	90	4.9
3.54	98	4.5
3.81	104	2.6
4.02	112	15.0
4.17	113	4.5
4.44	119	6.0
4.50	120	9.0
4.59	121	9.5
4.78	123	13.5
5.05	125	3.6
5.41	135	3.6
5.59	140	2.6
6.16	162	2.3
6.70	186	3.9
7.21	199	4.5
7.30	201	9.0
7.39	202	9.8
7.78	206	11.0
8.11	209	12.0
8.47	212	3.7
8.62	216	5.6
9.07	224	5.0
9.72	237	16.3
10.21	240	2.7
10.48	250	4.4
11.35	270	5.1
12.12	285	7.5
12.27	287	5.1
12.78	297	2.5
13.05	308	2.1
13.20	315	12.6
13.83	320	6.4
14.28	327	10.5
14.49	329	9.0
14.67	331	3.0

14.73	333	2.4
14.85	338	4.5
14.94	340	9.0
15.03	341	0.9
15.09	348	2.3
15.18	352	3.0
15.24	354	1.2
15.30	359	3.3
15.60	368	5.1
16.47	385	1.5
16.53	389	4.6
17.13	402	3.0
17.25	406	6.0
17.31	407	3.0
17.37	409	3.0
17.76	422	5.0
18.21	431	10.5
18.42	433	2.3
18.79	449	2.6
18.97	456	2.1
19.30	472	3.3
19.60	481	5.4
19.87	486	8.2
20.20	490	1.8
20.56	510	1.5
20.59	512	1.1
20.68	520	5.6
21.85	541	3.0
22.06	548	1.2
22.27	566	4.1
22.96	583	4.5
23.14	587	6.0
23.38	591	6.8
23.92	599	15.0
24.07	600	7.5
24.22	602	1.2
24.34	612	2.3
24.76	630	3.3
25.09	640	1.5
25.87	692	3.5
26.08	698	2.5
26.68	722	8.7
27.55	732	4.3
28.15	746	1.2
28.60	784	2.0
28.96	802	2.5
29.47	822	4.2
29.89	832	2.6
30.31	848	6.8
31.12	860	4.5

31.30	864	4.5
31.66	872	3.0
32.14	888	3.3
32.80	908	2.8
33.13	920	1.7
33.67	952	4.2
34.18	964	3.0
34.60	978	3.4
34.87	986	5.7
35.44	996	4.1
35.77	1004	2.2
36.16	1022	2.4
36.55	1038	3.0
36.67	1042	1.5
36.70	1044	0.9
36.82	1058	1.5
36.97	1068	6.8
37.24	1072	1.2
37.57	1100	1.5
37.69	1108	11.3
38.14	1112	2.7
38.41	1122	2.3
38.50	1126	1.7
39.10	1162	5.3
41.11	1200	5.7
42.94	1232	11.5
43.63	1238	1.1
43.81	1254	2.5
44.26	1272	9.6
45.22	1282	6.0
45.58	1288	4.1
46.57	1312	8.2
46.90	1316	5.3
47.11	1320	1.3
47.32	1336	2.1
47.65	1352	2.5
48.10	1370	2.6
48.31	1378	3.0
48.73	1392	7.5
49.03	1396	1.2
49.24	1414	1.5
49.72	1446	1.5
49.87	1456	10.9
50.74	1464	5.2
51.16	1472	2.6
51.58	1488	5.4
52.12	1498	0.7
52.27	1520	4.2
52.48	1525	3.0
52.78	1535	0.4

52.84	1550	1.9
53.08	1563	1.6
53.32	1578	1.9
53.56	1590	6.0
53.71	1593	2.6
54.04	1605	0.4
54.07	1613	0.9
54.16	1623	1.8
54.25	1628	0.9
54.34	1638	1.4
54.52	1650	1.8
54.61	1655	2.3
55.18	1680	8.5
57.10	1703	2.8
57.52	1718	5.6
57.94	1725	4.6
58.51	1738	2.4
58.75	1748	6.8
59.26	1755	9.0
60.16	1765	1.7
60.55	1788	3.0
60.70	1793	4.0
61.00	1800	3.4